



CPC 50th anniversary article

## Nektar++: Enhancing the capability and application of high-fidelity spectral/*hp* element methods<sup>☆,☆☆</sup>



David Moxey<sup>a,\*</sup>, Chris D. Cantwell<sup>b</sup>, Yan Bao<sup>c</sup>, Andrea Cassinelli<sup>b</sup>, Giacomo Castiglioni<sup>b</sup>, Sehun Chun<sup>d</sup>, Emilia Juda<sup>b</sup>, Ehsan Kazemi<sup>d</sup>, Kilian Lackhove<sup>f</sup>, Julian Marcon<sup>b</sup>, Gianmarco Mengaldo<sup>g</sup>, Douglas Serson<sup>b</sup>, Michael Turner<sup>b</sup>, Hui Xu<sup>e,b</sup>, Joaquim Peiró<sup>b</sup>, Robert M. Kirby<sup>h</sup>, Spencer J. Sherwin<sup>b</sup>

<sup>a</sup> College of Engineering, Mathematics and Physical Sciences, University of Exeter, United Kingdom

<sup>b</sup> Department of Aeronautics, Imperial College London, United Kingdom

<sup>c</sup> Department of Civil Engineering, Shanghai Jiao Tong University, Shanghai, China

<sup>d</sup> Underwood International College, Yonsei University, South Korea

<sup>e</sup> School of Aeronautics and Astronautics, Shanghai Jiao Tong University, Shanghai, China

<sup>f</sup> Department of Energy and Power Plant Technology, Technische Universität Darmstadt, Germany

<sup>g</sup> Division of Engineering and Applied Science, California Institute of Technology, USA

<sup>h</sup> Scientific Computing and Imaging Institute, University of Utah, USA

### ARTICLE INFO

#### Article history:

Received 4 June 2019

Received in revised form 26 November 2019

Accepted 5 December 2019

Available online 18 December 2019

#### Keywords:

Nektar++

Spectral/*hp* element methods

High-order finite element methods

### ABSTRACT

*Nektar++* is an open-source framework that provides a flexible, high-performance and scalable platform for the development of solvers for partial differential equations using the high-order spectral/*hp* element method. In particular, *Nektar++* aims to overcome the complex implementation challenges that are often associated with high-order methods, thereby allowing them to be more readily used in a wide range of application areas. In this paper, we present the algorithmic, implementation and application developments associated with our *Nektar++* version 5.0 release. We describe some of the key software and performance developments, including our strategies on parallel I/O, on *in situ* processing, the use of collective operations for exploiting current and emerging hardware, and interfaces to enable multi-solver coupling. Furthermore, we provide details on a newly developed Python interface that enables a more rapid introduction for new users unfamiliar with spectral/*hp* element methods, C++ and/or *Nektar++*. This release also incorporates a number of numerical method developments – in particular: the method of moving frames (MMF), which provides an additional approach for the simulation of equations on embedded curvilinear manifolds and domains; a means of handling spatially variable polynomial order; and a novel technique for quasi-3D simulations (which combine a 2D spectral element and 1D Fourier spectral method) to permit spatially-varying perturbations to the geometry in the homogeneous direction. Finally, we demonstrate the new application-level features provided in this release, namely: a facility for generating high-order curvilinear meshes called *NekMesh*; a novel new *AcousticSolver* for aeroacoustic problems; our development of a ‘thick’ strip model for the modelling of fluid–structure interaction (FSI) problems in the context of vortex-induced vibrations (VIV). We conclude by commenting on some lessons learned and by discussing some directions for future code development and expansion.

#### Program summary

Program Title: Nektar++

Program Files doi: <http://dx.doi.org/10.17632/9dtrxd9d8nx.1>

Code Ocean Capsule: <https://doi.org/10.24433/CO.9865757.v1>

Licensing provisions: MIT

Programming language: C++

External routines/libraries: Boost, METIS, FFTW, MPI, Scotch, PETSc, TinyXML, HDF5, OpenCASCADE, CWIPI

<sup>☆</sup> This paper and its associated computer program are available via the Computer Physics Communication homepage on ScienceDirect (<http://www.sciencedirect.com/science/journal/00104655>).

<sup>☆☆</sup> The review of this paper was arranged by Prof. N.S. Scott.

\* Corresponding author.

E-mail address: [d.moxey@exeter.ac.uk](mailto:d.moxey@exeter.ac.uk) (D. Moxey).

*Nature of problem:* The *Nektar++* framework is designed to enable the discretisation and solution of time-independent or time-dependent partial differential equations.

*Solution method:* spectral/*hp* element method

© 2019 The Author(s). Published by Elsevier B.V. This is an open access article under the CC BY license (<http://creativecommons.org/licenses/by/4.0/>).

## 1. Introduction

High-order finite element methods are becoming increasingly popular in both academia and industry, as scientists and technological innovators strive to increase the fidelity and accuracy of their simulations whilst retaining computational efficiency. The spectral/*hp* element method in particular, which combines the geometric flexibility of classical low-order finite element methods with the attractive convergence properties of spectral discretisations, can yield a number of advantages in this regard. From a numerical analysis perspective, their diffusion and dispersion characteristics mean that they are ideally suited to applications such as fluid dynamics, where flow structures must be convected across long time- and length-scales without suffering from artificial dissipation [1–5]. High-order methods are also less computationally costly than traditional low-order numerical schemes for a given number of degrees of freedom, owing to their ability to exploit a more locally compact and dense elemental operators when compared to sparse low-order discretisations [6–8]. In addition, high-order methods in various formulations can be seen to encapsulate other existing methods, such as finite volume, finite difference (e.g. summation-by-parts finite difference [9]), finite element, and flux reconstruction approaches [10, 11]. All of these features make the spectral/*hp* element method an extremely attractive tool to practitioners.

As the name suggests, the spectral/*hp* element method relies on the tessellation of a computational domain into a collection of elements of arbitrary size that form a mesh, where each element is equipped with a polynomial expansion of arbitrary and potentially spatially-variable order [12]. Within this definition, we include continuous Galerkin (CG) and discontinuous Galerkin (DG) methods, along with their variants. High-order methods have been historically seen as complex to implement, and their adoption has been consequently limited to academic groups and numerical analysts. This mantra is rapidly being removed thanks to the development of open-source numerical libraries that facilitate the implementation of new high-fidelity solvers for the solution of problems arising from a broad spectrum of research areas including engineering, biomedicine, economics, numerical weather and climate prediction. An additional challenge in the use of high-order methods, particularly for problems involving complex geometries, is the generation of a curvilinear mesh that conforms to the underlying curves and surfaces. However, advances in curvilinear mesh generation (such as [13]), combined with open-source efforts to increase their prevalence, mean that simulations across extremely complex geometries are now possible.

*Nektar++* is a project initiated in 2005 (the first commit to an online repository was made on 4th May 2006), with the aim of facilitating the development of high-fidelity computationally-efficient, and scalable spectral element solvers, thereby helping close the gap between application-domain experts (or users), and numerical-method experts (or developers). Along with *Nektar++*, other packages that implement such high-order methods have been developed in the past several years. *Nek5000*, developed at Argonne National Laboratory, implements CG discretisations mainly for solving incompressible and low-Mach number flow problems on hexahedral meshes using the classical spectral element method of collocated Lagrange interpolants [14]. *Semtex* [15,

16] is a fluid dynamics code that also uses the classical spectral element method in two dimensions, with the use of a 1D pseudospectral Fourier expansion for three dimensional problems containing a homogeneous component of geometry. *Nektar++* also supports this joint discretisation in Cartesian coordinates; however *Semtex* also includes support for cylindrical coordinate systems, where the Fourier modes are used in the azimuthal direction, which broadens the range of geometries that can be considered in this setting. *deal.II* [17] is a more generic finite element framework, which likewise restricts its element choices to quadrilaterals and hexahedra, but permits the solution of a wide array of problems, alongside the use of adaptive mesh refinement. *Flexi* [18] and its spinoff *Fluxo* [19], developed at the University of Stuttgart and at the University of Cologne, implement discontinuous Galerkin methods for flow problems on hexahedral meshes. *GNuME*, and its *NUMO* and *NUMA* components developed at the Naval Postgraduate School, implement both continuous and discontinuous Galerkin methods mainly for weather and climate prediction purposes [20,21]. *PyFR* [22], developed at Imperial College London, implements the flux reconstruction approach [23] which shares various numerical properties with DG in particular [10,24]. *DUNE* implements a DG formulation, among a wide variety of other numerical methods such as finite difference and finite volume methods [25].

*Nektar++* is a continuation of an earlier code *Nektar*, itself developed at Brown University originally using the C programming language, with some parts extended to use C++. *Nektar++* is instead written using the C++ language, and greatly exploits its object-oriented capabilities. The aim of *Nektar++* is to encapsulate many of the high-order discretisation strategies mentioned previously, in a readily accessible framework. The current release includes both CG and DG methods and, arguably, its distinguishing feature is its inherent support for complex geometries through various unstructured high-order element types; namely hexahedra, tetrahedra, prisms and pyramids for three-dimensional problems, and quadrilaterals and triangles for two-dimensional problems. Both CG and DG can be used on meshes that contain different element shapes (also referred to as hybrid meshes), and allow for curvilinear element boundaries in proximity of curved geometrical shapes. Along with these spatial discretisations, *Nektar++* supports so-called quasi-3D simulations in a manner similar to *Semtex*, where a geometrically complex 2D spectral element mesh is combined with a classical 1D Fourier expansion in a third, geometrically homogeneous, direction. This mixed formulation can significantly enhance computational efficiency for problems of the appropriate geometry [15] and *Nektar++* supports a number of different parallelisation strategies for this approach [26]. The time discretisation is achieved using a general linear method formulation for the encapsulation of implicit, explicit and mixed implicit–explicit timestepping schemes [27]. While the main purpose of the library is to create an environment under which users can develop novel solvers for the applications of their interest, *Nektar++* already includes fully-fledged solvers for the solution of several common systems, including fluid flows governed either by the compressible or incompressible Navier–Stokes and Euler equations; advection–diffusion–reaction problems, including on a manifold, with specific applications to cardiac electrophysiology [28]; a solver for various forms of the acoustic perturbation equations for aeroacoustic modelling; and others. One of the main shortcomings of the spectral/*hp* element method

is related to a perceived lack of robustness, arising from low dissipative properties, which can be a significant challenge for industrial applications. *Nektar++* implements several techniques to address this problem, namely efficient dealiasing strategies [29,30] and spectral vanishing viscosity [31], that have proved invaluable for particularly challenging applications [32].

The scope of this review is to highlight the substantial number of new developments in *Nektar++* since the last publication related to the software, released in 2015 and coinciding with the version 4 release of *Nektar++* [33]. Since this release, over 7000 commits have been added to the main code for the version 5 documented here, with a key focus on expanding the capability of the code to provide efficient high-fidelity simulations for challenging problems in various scientific and engineering fields. To this end, the paper is organised as follows. After a brief review of the formulation in Section 2, in Section 3 we present our software and performance developments. This includes our strategies on parallel I/O; *in situ* processing; the use of collective linear algebra operations for exploiting current and emerging hardware; and interfaces for multi-solver coupling to enable multi-physics simulations using *Nektar++*. Furthermore, we provide details on our new Python interfaces that enable more rapid on-boarding of new users unfamiliar with either spectral/*hp* element methods, C++ or *Nektar++*. In Section 4, we then present recent numerical method developments – in particular, the method of moving frames (MMF); recently added support for spatially-variable polynomial order for *p*-adaptive simulations; and new ways of incorporating global mappings to enable spatially variable quasi-3D approaches. In Section 5, we then demonstrate some of the new features provided in our new release, namely: our new facility for generating high-order (curvilinear) meshes called *NekMesh*; a new *AcousticSolver* for aeroacoustic problems; and our development of a ‘thick’ strip model for enabling the solution of fluid–structure interaction (FSI) problems in the context of vortex-induced vibrations (VIV). We conclude in Section 7 by commenting on some lessons learned and by discussing some directions for future code development and expansion.

**Contributors.** *Nektar++* has been developed across more than a decade, and we would like to acknowledge the many people who have made contributions to the specific application codes distributed with the libraries. In addition to the coauthors of the previous publication [33] we would like to explicitly thank the following for their contributions:

- Dr. Rheeda Ali (Department of Biomedical Engineering, Johns Hopkins University, USA) and Dr. Caroline Roney (Biomedical Engineering Department, King’s College London, UK) for their work on the cardiac electrophysiology solver;
- Dr. Michael Barbour and Dr. Kurt Sansom (Department of Mechanical Engineering, University of Washington, USA) for developments related to biological flows;
- Mr. Filipe Buscariolo (Department of Aeronautics, Imperial College London, UK) for contributions to the incompressible Navier–Stokes solver;
- Dr. Jeremy Cohen (Department of Aeronautics, Imperial College London, UK) for work relating to cloud deployment and the Nekkloud interface;
- Mr. Ryan Denny (Department of Aeronautics, Imperial College London, UK) for enhancements in the 1D arterial pulse wave model;
- Mr. Jan Eichstädt (Department of Aeronautics, Imperial College London, UK) for initial investigations towards using many-core and GPU platforms;
- Dr. Stanisław Gepner (Faculty of Power and Aeronautical Engineering, Warsaw University of Technology, Poland) for enhancements in the Navier–Stokes linear stability solver;

- Mr. Dav de St. Germain (SCI Institute, University of Utah, USA) for enhancements of timestepping schemes;
- Mr. Ashok Jallepalli (SCI Institute, University of Utah, USA) for initial efforts on the integration of SIAC filters into post-processing routines;
- Prof. Dr. Johannes Janicka (Department of Energy and Power Plant Technology), Technische Universität Darmstadt, Germany, for support and development of the acoustic solver and solver coupling;
- Mr. Edward Laughton (College of Engineering, Mathematics and Physical Sciences, University of Exeter, UK) for testing enhancements and initial efforts on non-conformal grids;
- Dr. Rodrigo Moura (Divisão de Engenharia Aeronáutica, Instituto Tecnológico de Aeronáutica, Brasil) for numerical developments related to spectral vanishing viscosity stabilisation;
- Dr. Rupert Nash and Dr. Michael Bareford (EPCC, University of Edinburgh, UK) for their work on parallel I/O; and
- Mr. Zhenguo Yan and Mr. Yu Pan (Department of Aeronautics, Imperial College London, UK) for development of the compressible flow solver;

## 2. Methods

In this first section, we outline the mathematical framework that underpins *Nektar++*, as originally presented in [33,34]. *Nektar++* supports a variety of spatial discretisation choices, primarily based around the continuous and discontinuous Galerkin methods (CG and DG). However, in the majority of cases CG and DG use the same generic numerical infrastructure. Here we therefore present a brief overview and refer the reader to [12] for further details, which contains a comprehensive description of the method and its corresponding implementation choices. In the text below we also highlight appropriate chapters and sections from [12] for the material being discussed.

The broad goal of *Nektar++* is to provide a framework for the numerical solution of partial differential equations (PDEs) of the form  $\mathcal{L}u = 0$  on a domain  $\Omega$ , which may be geometrically complex, for some solution  $u$ . Practically, in order to carry out a spatial discretisation of the PDE problem,  $\Omega$  needs to be partitioned into a finite number of  $d$ -dimensional non-overlapping elements  $\Omega_e$ , where in *Nektar++* we support  $1 \leq d \leq 3$ , such that the collection of all elements recovers the original region ( $\Omega = \bigcup \Omega_e$ ) and for  $e_1 \neq e_2$ ,  $\Omega_{e_1} \cap \Omega_{e_2} = \partial\Omega_{e_1e_2}$  is an empty set or an interface of dimension  $\bar{d} < d$ . The domain may be embedded in a space of equal or higher dimension,  $\hat{d} \geq d$ , as described in [28]. One of the distinguishing features of *Nektar++* is that it supports a wide variety of elemental shapes: namely segments in one dimension [12, §2]; triangles and quadrilaterals in two dimensions, and; tetrahedra, pyramids, prisms and hexahedra in three dimensions [12, §3 and §4]. This makes it broadly suitable for the solution of problems in complex domains, in which hybrid meshes of multiple elements are generally required.

*Nektar++* supports the solution of PDE systems that are either steady-state or time-dependent. In time-dependent cases, there is subsequently a choice to use either explicit, implicit or implicit–explicit timestepping. From an implementation and formulation perspective, steady-state and implicit-type problems typically require the efficient solution of a system of linear equations, whereas explicit-type problems rely on the evaluation of the spatially discretised mathematical operators. In the following sections, we briefly outline the support in *Nektar++* for these regimes.



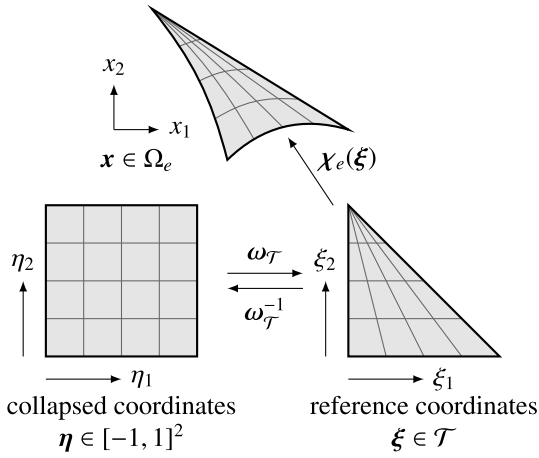


**Fig. 1.** Coordinate systems and mappings between collapsed coordinates  $\eta$ , reference coordinates  $\xi$  and Cartesian coordinates  $\mathbf{x}$  for a high-order triangular element  $\Omega_e$ .

### 2.1. Implicit-type methods

In this approach we follow the standard finite element derivation as described in [12, §2.2], so that before establishing the spatial discretisation, the abstract operator form  $\mathcal{L}u = 0$  is formulated in the weak sense alongside appropriate test and trial spaces  $\mathcal{V}$  and  $\mathcal{U}$ . In general, we require at least a first-order derivative and select, for example,  $\mathcal{V} = H_0^1(\Omega) := \{v \in H^1(\Omega) \mid v(\partial\Omega) = 0\}$ , where

$$H^1(\Omega) := \{v \in L^2(\Omega) \mid D^\alpha u \in L^2(\Omega) \forall |\alpha| \leq 1\}.$$

Following the Galerkin approach, we select  $\mathcal{U} = \mathcal{V}$ . We note that where problems involve Dirichlet boundary conditions on a boundary  $\partial\Omega_D \subset \partial\Omega$  of the form  $u|_{\partial\Omega_D}(\mathbf{x}) = g_D(\mathbf{x})$ , we typically enforce this by lifting  $g_D$  as described in [12, §2.2.3 and §4.2.4]. For illustrative purposes, we assume that  $\mathcal{L}$  is linear and its corresponding weak form can be expressed as: *find*  $u \in \mathcal{U}$  such that

$$a(u, v) = \ell(v) \quad \forall v \in \mathcal{U}, \quad (1)$$

where  $a(\cdot, \cdot)$  is a bilinear form and  $\ell(\cdot)$  is a linear form.

To numerically solve the problem given in Eq. (1) with the spatial partition of  $\Omega$ , we consider solutions in an appropriate finite-dimensional subspace  $\mathcal{U}_N \subset \mathcal{U}$ . In a high-order setting, these spaces correspond to the choice of spatial discretisation on the mesh. For example, in the discontinuous setting we select

$$\mathcal{U}_N = \{u \in L^2(\Omega) \mid u|_{\Omega_e} \in \mathcal{P}_p(\Omega_e)\},$$

where  $\mathcal{P}_p(\Omega_e)$  represents the space of polynomials on  $\Omega_e$  up to total degree  $P$ , so that functions are permitted to be discontinuous across elemental boundaries. In the continuous setting, we select the same space intersected with  $C^0(\Omega)$ , so that expansions are continuous across elemental boundaries. The solution to the weak form in Eq. (1) can then be cast as: *find*  $u^\delta \in \mathcal{U}_N$  such that

$$a(u^\delta, v^\delta) = \ell(v^\delta) \quad \forall v^\delta \in \mathcal{U}_N \quad (2)$$

Assuming that the solution can be represented as  $u^\delta(\mathbf{x}) = \sum_n \hat{u}_n \Phi_n(\mathbf{x})$ , a weighted sum of  $N$  trial functions  $\Phi_n(\mathbf{x}) \in \mathcal{U}_N$  defined on  $\Omega$  [12, §2.1], the problem then becomes that of finding the coefficients  $\hat{u}_n$ , which in the Galerkin approach translates into the solution of a system of linear equations.

To establish the global basis  $\Phi(\Omega) = \{\Phi_1(\mathbf{x}), \dots, \Phi_N(\mathbf{x})\}$ , we first consider the contributions from each element in the domain. To simplify the definition of basis functions on each element, we follow the standard approach described in [12, §2.3.1.2 and §4.1.3] where  $\Omega_e$  is mapped from a reference element  $\mathcal{E} \subset [-1, 1]^d$  by

**Table 1**

List of supported elemental reference regions.

Name	Class	Domain definition
Segment	StdSeg	$\mathcal{S} = \{\xi_1 \in [-1, 1]\}$
Quadrilateral	StdQuad	$\mathcal{Q} = \{\xi \in [-1, 1]^2\}$
Triangle	StdTri	$\mathcal{T} = \{\xi \in [-1, 1]^2 \mid \xi_1 + \xi_2 \leq 0\}$
Hexahedron	StdHex	$\mathcal{H} = \{\xi \in [-1, 1]^3\}$
Prism	StdPrism	$\mathcal{R} = \{\xi \in [-1, 1]^3 \mid \xi_1 \leq 1, \xi_2 + \xi_3 \leq 0\}$
Pyramid	StdPyr	$\mathcal{P} = \{\xi \in [-1, 1]^3 \mid \xi_1 + \xi_3 \leq 0, \xi_2 + \xi_3 \leq 0\}$
Tetrahedron	StdTet	$\mathcal{A} = \{\xi \in [-1, 1]^3 \mid \xi_1 + \xi_2 + \xi_3 \leq -1\}$

a parametric mapping  $\chi_e : \mathcal{E} \rightarrow \Omega_e$ , so that  $\mathbf{x} = \chi_e(\xi)$ . Here,  $\mathcal{E}$  is one of the supported region shapes in Table 1 and  $\xi$  are  $d$ -dimensional coordinates representing positions in a reference element, distinguishing them from  $\mathbf{x}$  which are  $d$ -dimensional coordinates in the Cartesian coordinate space. On triangular, tetrahedral, prismatic and pyramid elements, one or more of the coordinate directions of a quadrilateral or hexahedral region are collapsed to form the appropriate reference shape, creating one or more singular vertices within these regions [35,36]. Operations, such as calculating derivatives, map the tensor-product coordinate system to these shapes through Duffy transformations [37] – for example,  $\omega_{\mathcal{T}} : \mathcal{T} \rightarrow \mathcal{Q}$  maps the triangular region  $\mathcal{T}$  to the quadrilateral region  $\mathcal{Q}$  – to allow these methods to be well-defined. The relationship between these coordinates is depicted in Fig. 1. Note that the singularity in the inverse mapping  $\omega_{\mathcal{T}}^{-1}$  does not affect convergence order and can be mitigated in practice by adopting an alternative choice of quadrature, such as Gauss–Radau points, in order to omit the collapsed vertices [12, §4.1.1].

The mapping  $\chi_e$  need not necessarily exhibit a constant Jacobian, so that the resulting element is deformed as shown in Fig. 1. *Nektar++* represents the curvature of these elements by taking a sub- or iso-parametric mapping for  $\chi_e$ , so that the curvature is defined using at least a subset of the basis functions used to represent the solution field [12, §4.3.5]. The ability to use such elements in high-order simulations is critical in the simulation of complex geometries, as without curvilinear elements, one could not accurately represent the underlying curves and surfaces of the geometry, as demonstrated in [38]. The generation of meshes involving curved elements is, however, a challenging problem. Our efforts to generate such meshes, as well as to adapt linear meshes for high-order simulations, are implemented in the *NekMesh* generator tool described in Section 5.1, as well as a number of recent publications (e.g. [13,39]).

With the mapping  $\chi_e$  and the transformation  $\omega_{\mathcal{T}}$  the discrete approximation  $u^\delta$  to the solution  $u$  on a single element  $\Omega_e$  can then be expressed as

$$u^\delta(\mathbf{x}) = \sum_n \hat{u}_n \phi_n \left( [\chi_e]^{-1}(\mathbf{x}) \right)$$

where  $\phi_n$  form a basis of  $\mathcal{P}_p(\mathcal{E})$ ; i.e. a local polynomial basis need only be constructed on each reference element. A one-dimensional order- $P$  basis is a set of polynomials  $\phi_p(\xi)$ ,  $0 \leq p \leq P$ , defined on the reference segment,  $\mathcal{S}$ . The choice of basis is usually made based on its mathematical or numerical properties and may be modal or nodal in nature [12, §2.3]. For two- and three-dimensional regions, a tensorial basis may be employed, where the polynomial space is constructed as the tensor-product of one-dimensional bases on segments, quadrilaterals or hexahedral regions. In spectral/*hp* element methods, a common choice is to use a modified hierarchical Legendre basis (a ‘bubble’-like polynomial basis sometimes referred to as the ‘modal basis’), given in [12, §3.2.3] as a function of one variable by

$$\phi_p(\xi) = \begin{cases} \frac{1-\xi}{2} & p = 0, \\ \left(\frac{1-\xi}{2}\right) \left(\frac{1+\xi}{2}\right) P_{p-1}^{1,1}(\xi) & 0 < p < P, \\ \frac{1+\xi}{2} & p = P, \end{cases}$$

which supports boundary–interior decomposition and therefore improves numerical efficiency when solving the globally assembled system. Equivalently,  $\phi_p$  could also be defined by the Lagrange polynomials through the Gauss-Lobatto-Legendre quadrature points, which would lead to a traditional spectral element method [12, §2.3.4]. In higher dimensions, a tensor product of either basis can be used on quadrilateral and hexahedral elements respectively. On the other hand, the use of a collapsed coordinate system also permits the use of a tensor product modal basis for the triangle, tetrahedron, prism and pyramid, which when combined with tensor contraction techniques can yield performance improvements. This aspect is considered further in Section 3.3 and [40,41].

Elemental contributions to the solution may be assembled to form a global solution through an assembly operator [12, §2.3.1 and §4.2.1]. In a continuous Galerkin setting, the assembly operator sums contributions from neighbouring elements to enforce the  $C^0$ -continuity requirement. In a discontinuous Galerkin formulation, such mappings transfer flux values from the element interfaces into the global solution vector. For elliptic operators, *Nektar++* has a wide range of implementation choices available to improve computational performance. A common choice is the use of a (possibly multi-level) static condensation of the assembled system [12, §4.1.6 and §4.2.3], where a global system is formed only on elemental boundary degrees of freedom. This is supported both for the classical continuous framework, as well as in the DG method. In the latter, this gives rise to the hybridisable discontinuous Galerkin (HDG) approach [42], in which a global system is solved on the trace or skeleton of the overall mesh.

## 2.2. Explicit-type methods

*Nektar++* has extensive support for the solution of problems in a time-explicit manner, which requires the evaluation of discretised spatial operators alongside projection into the appropriate space. As the construction of the implicit operators requires these same operator evaluations, most of the formulation previously discussed directly translates to this approach. We do note however that there is a particular focus on the discontinuous Galerkin method as shown in [12, §6.2] for multi-dimensional hyperbolic systems of the form

$$\frac{d\mathbf{u}}{dt} + \nabla \cdot \mathbf{F}(\mathbf{u}) = \mathbf{G}(\mathbf{u}).$$

This includes the acoustic perturbation equations that we discuss in Section 5.2 and the compressible Navier–Stokes system used for aerodynamics simulations in Section 5.4. In this setting, on a single element, and further assuming  $\mathbf{G}$  is zero for simplicity of presentation as in [12, §6.2.2], we multiply the above equation by an appropriate test function  $v \in \mathcal{U}$  and integrate by parts to obtain

$$\int_{\Omega_e} \frac{d\mathbf{u}}{dt} v \, d\mathbf{x} + \int_{\partial\Omega_e} v \tilde{\mathbf{f}}^e(\mathbf{u}^-, \mathbf{u}^+) \cdot \mathbf{n} \, ds - \int_{\Omega_e} \nabla v \cdot \mathbf{F}(\mathbf{u}) \, d\mathbf{x} = 0.$$

In the above,  $\tilde{\mathbf{f}}^e(\mathbf{u}^-, \mathbf{u}^+)$  denotes a numerically calculated boundary flux, depending on the element-interior velocity  $\mathbf{u}^-$  and its neighbour's velocity  $\mathbf{u}^+$ . The choice of such a flux is solver-specific and may involve an upwinding approach or use of an appropriate Riemann solver. Where second-order diffusive terms are required, *Nektar++* supports the use of a local discontinuous Galerkin (LDG) approach to minimise the stencil required for communication (see [43] and [12, §7.5.2]). From a solver perspective, the implementation of the above is fairly generic, requiring only the evaluation of the flux term  $\tilde{\mathbf{f}}$ , conservation law  $\mathbf{F}(\mathbf{u})$  and right-hand side source terms  $\mathbf{G}(\mathbf{u})$ .

## 2.3. Recap of Nektar++ implementation

In this section, we briefly outline the implementation of these methods inside *Nektar++*. Further details on the overall design of *Nektar++*, as well as examples of how to use it, can be found in the previous publication [33].

The core of *Nektar++* comprises six libraries which are designed to emulate the general mathematical formulation expressed above. They describe the problem in a hierarchical manner, by working from elemental basis functions and shapes through to a C++ representation of a high-order field and complete systems of partial differential equations on a complex computational domain. Depending on the specific application, this then allows developers to choose an appropriate level for their needs, balancing ease of use at the highest level with fine-level implementation details at the lowest. A summary of each library's purpose is the following:

- **LibUtilites**: elemental basis functions  $\psi_p$ , quadrature point distributions  $\xi_i$  and basic building blocks such as I/O handling;
- **StdRegions**: reference regions  $\mathcal{E}$  along with the definition of key finite element operations across them, such as integration, differentiation and transformations;
- **SpatialDomains**: the geometric mappings  $\chi_e$  and factors  $\frac{\partial \chi}{\partial \xi}$ , as well as Jacobians of the mappings and the construction of the topology of the mesh from the input geometry;
- **LocalRegions**: physical regions in the domain, composing a reference region  $\mathcal{E}$  with a map  $\chi_e$ , extensions of core operations onto these regions;
- **MultiRegions**: list of physical regions comprising  $\Omega$ , global assembly maps which may optionally enforce continuity, construction and solution of global linear systems, extension of local core operations to domain-level operations; and
- **SolverUtils**: building blocks for developing complete solvers.

In version 5.0, four additional libraries have been included. Each of these can be seen as a non-core, in the sense that they provide additional functionality to the core libraries above:

- **Collections**: encapsulates the implementation of key kernels (such as inner products and transforms) with an emphasis on evaluating operators collectively for similar elements;
- **GlobalMapping**: implements a mapping technique that allows quasi-3D simulations (i.e. those using a hybrid 2D spectral element/1D Fourier spectral discretisation) to define spatially-inhomogeneous deformations;
- **NekMeshUtils**: contains interfaces for CAD engines and key mesh generation routines, to be used by the *NekMesh* mesh generator; and
- **FieldUtils**: defines various post-processing modules that can be used both by the post-processing utility *FieldConvert*, as well as solvers for in-situ processing.

We describe the purpose of these libraries in greater detail in Sections 3.3, 4.3, 5.1 and 3.2 respectively.

## 3. Software and performance developments

This section reviews the software and performance developments added to *Nektar++* since our last major release. We note that a significant change from previous releases is the use of C++11-specific language features throughout the framework. A brief summary of our changes in this area include:

- transitioning from various data structures offered in boost to those now natively available in C++11: in particular, smart pointers such as `shared_ptr`, unordered STL containers and function bindings;

- avoid the use of typedef aliases for complex data structure types, in deference to the use of auto where appropriate;
- similarly, where appropriate we make use of range-based for loops to avoid iterator typedef usage and simplify syntax;
- use of variadic templates in core memory management and data structures to avoid the use of syntax-dense preprocessing macros at compile time.

Alongside the many developments outlined here, the major change in the *Nektar++* API resulting from this switch has further motivated the release of a new major version of the code. The developments described in this section are primarily geared towards our continuing efforts to support our users on large-scale high-performance computing (HPC) systems.

### 3.1. Parallel I/O

Although the core of *Nektar++* has offered efficient parallel scaling for some time (as reported in previous work [33]), one aspect that has been improved substantially in the latest release is support for parallel I/O, both during the setup phase of the simulation and when writing checkpoints of field data for unsteady simulations. In both cases, we have added support for new, parallel-friendly mesh input files and data checkpoint files that use the HDF5 file format [44], in combination with Message Passing Interface (MPI) I/O, to significantly reduce bottlenecks relating to the use of parallel filesystems. This approach enables *Nektar++* to either read or write a single file across all processes, as opposed to a file-per-rank output scheme that can place significant pressure on parallel filesystems, particularly during the partitioning phase of the simulation. Here we discuss the implementation of the mesh input file format; details regarding the field output can be found in [45].

One of the key challenges identified in the use of *Nektar++* within large-scale HPC environments is the use of an XML-based input format used for defining the mesh topology. Although XML is highly convenient from the perspective of readability and portability, particularly for small simulations, the format does pose a significant challenge at larger scales, since when running in parallel there is no straightforward way to extract a part of an XML file on each process. This means that in the initial phase of the simulation, where the mesh is partitioned into smaller chunks that run on each process, there is a need for at least one process to read the entire XML file. Even at higher orders, where meshes are typically coarse to reflect the additional degrees of freedom in each element, detailed simulations of complex geometries typically require large, unstructured meshes of millions of high-order elements. Having only a single process read this file therefore imposes a natural limit to the strong scaling of the setup phase of simulations – that is, the maximum number of processes that can be used – due to the large memory requirement and processing time to produce partitioned meshes. It also imposes potentially severe restrictions on start-up time of simulations and/or the post-processing of data, hindering throughput for very large cases.

Although various approaches have been used to partially mitigate this restriction, such as pre-partitioning the mesh before the start of the simulation and utilising a compressed XML format that reduces file sizes and the XML tree size, these do not themselves cure the problem entirely. In the latest version of *Nektar++* we address this issue with a new Hierarchical Data Format v5 (HDF5) file format. To design the layout of this file, we recall that the structure of a basic *Nektar++* mesh requires the following storage:

- Vertices of the mesh are defined using double-precision floating point numbers for their three coordinates. Each vertex has a unique ID.

- All other elements are defined using integer IDs in a hierarchical manner; for example in three dimensions edges are formed from pairs of vertices, faces from 3 or 4 edges and elements from a collection of faces.

This hierarchical definition clearly aligns with the HDF5 data layout. To accommodate the ‘mapping’ of a given ID into a tuple of IDs or vertex coordinates, we adopt the following basic structure:

- The mesh group contains multi-dimensional datasets that define the elements of a given dimension. For example, given  $N$  quadrilaterals, the quad dataset within the mesh group is a  $N \times 4$  dataset of integers, where each row denotes the 4 integer IDs of edges that define that quadrilateral.
- The maps group contains one-dimensional datasets that define the IDs of each row of the corresponding two-dimensional dataset inside mesh.

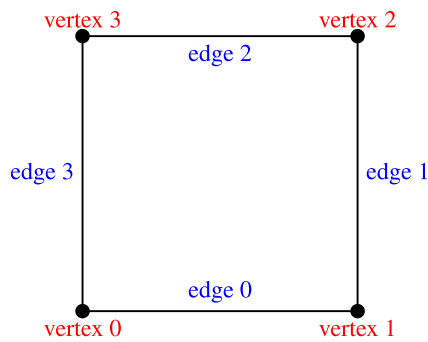
An example of this structure for a simple quadrilateral mesh is given in Fig. 2. We also define additional datasets to define element curvature and other ancillary structures such as boundary regions.

When running in parallel, *Nektar++* adopts a domain decomposition strategy, whereby the mesh is partitioned into a subset of the whole domain for each process. This can be done either at the start of the simulation, or prior to running it. Parallelisation is achieved using the standard MPI protocol, where each process is independently executed and there is no explicit use of shared memory in program code. Under the new HDF5 format, we perform a parallel partitioning strategy at startup, which runs as follows:

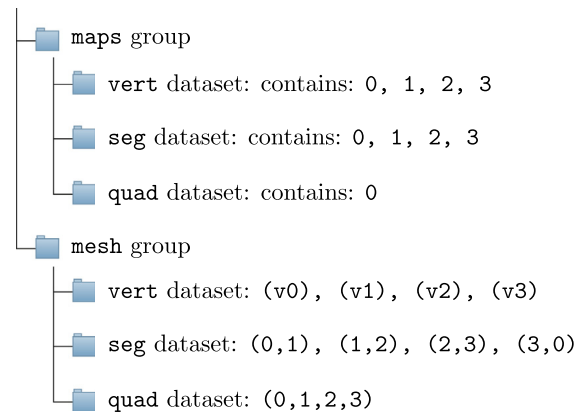
- Each process is initially assigned a roughly equal number of elements to read. This is calculated by querying the size of each elemental dataset to determine the total number of elements, and then partitioned equally according to the rank of the process and total number of processors.
- The dual graph corresponding to each process’ subdomain is then constructed. Links to other process subdomains are established by using ghost nodes to those process’ nodes.
- The dual graph is passed to the PT-Scotch library [46] to perform partitioning in parallel on either the full system or a subset of processes, depending on the size of the graph.
- Once the resulting graph is partitioned, the datasets are read in parallel using a top-down process: i.e. in three dimensions, we read the volumes, followed by faces, edges and finally vertices. In the context of Fig. 2, this would consist of reading the quad dataset, followed by the *seg* dataset, followed by the *vert* dataset.
- Note that at each stage, each processor only reads the geometric entities that are required for its own partition, which is achieved through the use of HDF5 selection routines when reading the datasets.
- The *Nektar++* geometry objects are then constructed from these data in a bottom-up manner: i.e. vertices, followed by edges, followed by faces and finally volumes, as required by each processor.
- This concludes the construction of the linear mesh: curvature information is stored in separate datasets, and is also read at this stage as required for each element.
- Finally, ancillary information such as composites and domain definition are read from the remaining datasets.

The new HDF5 based format is typically significantly faster than the existing XML format to perform the initial partitioning phase of the simulation. Notably, whereas execution times for the XML format increase with the number of nodes being used (likely owing to the file that must be written for each rank by the root processor), the HDF5 input time remains roughly constant. We





(a) A simple two-dimensional quadrilateral mesh consisting of a single element.



(b) Directory-dataset structure that is used for storage of the topological data in the left-hand figure.

**Fig. 2.** An example of a single quadrilateral element grid. In (a), we show the topological decomposition of the element into its 4 edges and vertices. Figure (b) shows a schematic of the filesystem-type structure implemented in HDF5 that is used for storage of this topological information.

note that the HDF5 format also provides benefits for the post-processing of large simulation data, as the *FieldConvert* utility is capable of using this format for parallel post-processing of data.

### 3.2. In-situ processing

The increasing capabilities of high-performance computing facilities allow us to perform simulations with a large number of degrees of freedom, which leads to challenges in terms of post-processing. The first problem arises when we consider the storage requirements of the complete solution of these simulations. Tasks such as generating animations, where we need to consider the solution at many time instances, may become infeasible if we have to store the complete fields at each time instance. Another difficulty occurs due to the memory requirements of loading the solution for post-processing. Although this can be alleviated by techniques such as subdividing the data and processing one subdivision at a time, this is not possible for some operations requiring global information, such as performing a  $C^0$ -projection that involves the inversion of a global mass matrix. In such cases, the memory requirements might force the user to perform post-processing using a number of processing nodes similar to that used for the simulation.

To aid in dealing with this issue, *Nektar++* now supports processing the solution *in situ* during the simulation. The implementation of this feature was facilitated by the modular structure of our post-processing tool, *FieldConvert*. This tool uses a pipeline of modules, passing mesh and field data between them, to arrive at a final output file. This comprises one or more input modules (to read mesh and field data), zero or more processing modules (to manipulate the data, such as calculating derived quantities or extracting boundary information), and a single output module (to write the data in one of a number of field and visualisation formats). To achieve *in situ* processing, *FieldConvert* modules were moved to a new library (*FieldUtils*), allowing them to be executed during the simulation as well as shared with the *FieldConvert* utility. The actual execution of the modules during *in situ* processing is performed by a new subclass of the *Filter* class, which is called periodically after a prescribed number of time-steps to perform operations which do not modify the solution field. This filter structure allows the user to choose which modules should be used and to set configuration parameters. Multiple instances of the filter can be used if more than one post-processing pipeline is desired.

There are many example applications for this new feature. The most obvious is to generate a field or derived quantity, such as vorticity, as the simulation is running. An example of this is given in the supplementary materials Example A.16, in which the vorticity is calculated every 100 timesteps whilst removing the velocity and pressure fields to save output file space, using the following *FILTER* configuration in the session file:

```

1 <FILTER TYPE="FieldConvert">
2 <PARAM NAME="OutputFile"> vorticity.vtu </PARAM>
3 <PARAM NAME="OutputFrequency"> 100 </PARAM>
4 <PARAM NAME="Modules">
5   vorticity
6   removefield:fieldname=u,v,p
7 </PARAM>
8 </FILTER>

```

This yields a number of parallel-format block-unstructured VTK files (the VTU format), as described in [47], that can be visualised in appropriate applications such as ParaView [48] and subsequently assembled to form an animation. Other use cases include extracting slices or isocontours of the solution at several time instants for creating an animation. Since the resulting files are much smaller than the complete solution, there are significant savings in terms of storage when compared to the traditional approach of obtaining checkpoints which are later post-processed. Another possibility is to perform the post-processing operations after the last time-step, but before the solver returns. This way, it is possible to avoid the necessity of starting a new process which will have to load the solution again, leading to savings in computing costs.

### 3.3. Collective linear algebra operations

One of the primary motivations for the use of high-order methods is their ability to outperform standard linear methods on modern computational architectures in terms of equivalent error per degree of freedom. Although the cost in terms of floating point operations (FLOPS) of calculating these degrees of freedom increases with polynomial order, the dense, locally-compact structure of higher-order operators lends itself to the current hardware environment, in which FLOPS are readily available but memory bandwidth is highly limited. In this setting, the determining factor in computational efficiency, or ability to reach peak performance of hardware, is the arithmetic intensity of the method; that is, the number of FLOPS performed for each byte of data transferred over the memory bus. Algorithms need to have high arithmetic

intensity in order to fully utilise the computing power of modern computational hardware.

However, the increase in FLOPS at higher polynomial orders must be balanced against the desired accuracy so that execution times are not excessively high. An observation made early in the development of spectral element methods is that operator counts can be substantially reduced by using a combination of a tensor product basis, together with a tensor contraction technique referred to as *sum-factorisation*. This technique, exploited inside of *Nektar++* as well as other higher-order frameworks such as deal.II [17] and Nek5000, uses a small amount of temporary storage to reduce operator counts from  $\mathcal{O}(P^{2d})$  to  $\mathcal{O}(P^{d+1})$  at a given order  $P$ . For example, consider a polynomial interpolation on a quadrilateral across a tensor product of quadrature points  $\xi = (\xi_{1i}, \xi_{2j})$ , where the basis admits a tensor product decomposition  $\phi_{pq}(\xi) = \phi_p(\xi_1)\phi_q(\xi_2)$ . This expansion takes the form

$$\begin{aligned} u^\delta(\xi_{1i}, \xi_{2j}) &= \sum_{p=0}^P \sum_{q=0}^Q \hat{u}_{pq} \phi_p(\xi_{1i}) \phi_q(\xi_{2j}) \\ &= \sum_{p=0}^P \phi_p(\xi_{1i}) \left[ \sum_{q=0}^Q \hat{u}_{pq} \phi_q(\xi_{2j}) \right]. \end{aligned}$$

By precomputing the bracketed term and storing it for each  $p$  and  $j$ , we can reduce the number of floating point operations from  $\mathcal{O}(P^4)$  to  $\mathcal{O}(P^3)$ . One of the distinguishing features of *Nektar++* is that these types of basis functions are defined not only for tensor-product quadrilaterals and hexahedra, but also unstructured elements (triangles, tetrahedra, prisms and pyramids) through the use of a collapsed coordinate system and appropriate basis functions. For more details on this formulation, see [12].

The efficient implementation of the above techniques on computational hardware still poses a significant challenge for practitioners of higher-order methods. For example, *Nektar++* was originally designed using a hierarchical, inheritance-based approach, where memory associated with elemental degrees of freedom is potentially scattered non-contiguously in memory. Although this was appropriate at the initial time of development a decade ago, in modern terms this does not align with the requirements for optimal performance, in which large blocks of memory should be transferred and as many operations acted on sequentially across elements, so as to reduce memory access and increase data locality and cache usage. The current efforts of the development team are therefore focused on redesigns to the library to accommodate this process. In particular, since version 4.1, *Nektar++* has included a library called *Collections* which is designed to provide this optimisation. In the hierarchy of *Nektar++* libraries, *Collections* sits between *LocalRegions*, which represent individual elements, and *MultiRegions*, which represent their connection in either a  $C^0$  or discontinuous Galerkin setting. The purpose of the library, which is described fully in [40], is to facilitate optimal linear algebra strategies for large groupings of elements that are of the same shape and utilise the same basis. To facilitate efficient execution across a broad range of polynomial orders, we then consider a number of implementation strategies including:

- **StdMat**: where a full-rank matrix of the operator on a standard element is constructed, so that the operator can be evaluated with a single matrix-matrix multiplication;
- **IterPerExp**: where the sum-factorisation technique is evaluated using an iteration over each element, but geometric factors (e.g.  $\partial \mathbf{x} / \partial \xi$ ) are amalgamated between elements; and
- **SumFac**: where the sum-factorisation technique is evaluated across multiple elements concurrently.

This is then combined with an autotuning strategy, run at simulation startup, which attempts to identify the fastest evaluation strategy depending on characteristics of the computational mesh and basis parameters. Autotuning can be enabled in any simulation through the definition of an appropriate tag inside the NEKTAR block that defines a session file:

```
1 <COLLECTIONS DEFAULT="auto" />
```

A finer-grained level of control over the Collections setup and implementation strategies is documented in the user guide. Performance improvements using collections are most readily seen in fully-explicit codes such as the *CompressibleFlowSolver* and *AcousticSolver*. The vortex pair example defined in Section 5.2 and provided in Example A.15 demonstrates the use of the collections library.

### 3.4. Solver coupling

The *Nektar++* framework was extended with a coupling interface [49] that enables sending and receiving arbitrary variable fields at run time. Using such a technique, a coupling-enabled solver can exchange data with other applications to model multi-physics problems in a co-simulation setup. Currently, two coupling interfaces are available within *Nektar++*; a file-based system for testing purposes, and an MPI-based implementation for large-scale HPC implementations. The latter was designed to facilitate coupling *Nektar++* solvers with different software packages which use other discretisation methods and operate on vastly different time- and length-scales. To couple two incompatible discretisations, an intermediary expansion is used which can serve as a projection between both sides of the field. Coupling is achieved by introducing an intermediate expansion, which uses the same polynomial order and basis definitions as the parent *Nektar++* solver; however, a continuous projection and a larger number of quadrature points than the original expansion of the *Nektar++* solver are used. Based on this intermediate representation, the coupling strategy is comprised of three major steps:

- **Step 1**: The field values are requested from the sending application at the intermediate expansion's quadrature points. Here, aliasing can be effectively avoided by an appropriate selection of quadrature order and distribution. Point values that lie outside of the senders' computational domain can be either replaced by a default value or extrapolated from their available nearest neighbour.
- **Step 2**: The physical values at the quadrature points are then transformed into modal space. This is achieved by a modified forward transform that involves the differential low-pass filter [50]:

$$u^{**} - \left( \frac{\Delta \lambda}{2\pi} \right)^2 \nabla^2 u^{**} = u^*, \quad \frac{\partial u^{**}}{\partial x_i} \Big|_{\partial \Omega} = 0 \quad (3)$$

where  $u^*$  denotes the received field,  $u^{**}$  the filtered field and  $\Delta \lambda$  the user specified filter width. The filter removes small scale features *a priori* and thus reduces the error associated with the transform. Moreover, it does not add unwanted discontinuities at the element boundaries and imposes a global smoothing, due to the continuity of the intermediate expansion.

- **Step 3**: A linear interpolation in time can be performed to overcome larger time scales of the sending application. Due to their identical expansion bases and orders, the resulting coefficients can be directly used in the original expansion of the solver.



As is evident from the above strategy, sending fields to other solvers only requires an application to provide discrete values at the requested locations. In *Nektar++*, this can be achieved by evaluating the expansions or by a simpler approximation from the immediately available quadrature point values. All processing is performed by the receiver. The complex handling of data transfers is accomplished by the open-source CWIPI library [51], which enables coupling of multiple applications by using decentralised communication. It is based purely on MPI calls, has bindings for C, Fortran and Python, handles detection of out-of-domain points and has been shown to exhibit good performance [52]. With only CWIPI as a dependency and a receiver-centric strategy that can be adjusted to any numerical setup, the implementation of compatible coupling interfaces is relatively straightforward.

An example result of a transferred field is given in Fig. 3. For a hybrid noise simulation [49], the acoustic source term depicted at the top was computed by a proprietary, finite volume flow solver on a high-resolution mesh ( $\Delta h < 1.4$  mm) and transferred to the *Nektar++* *AcousticSolver*, which we describe in Section 5.2. After sampling, receiving, filtering, projection and temporal interpolation, the extrema of the source term are cancelled out and blurred by the spatial filter. Consequently, a much coarser mesh ( $\Delta h = 20$  mm) with a fourth order expansion is sufficient for the correct representation of the resulting field, which significantly reduces the computational cost of the simulation. The corresponding loss of information is well defined by the filter width  $\Delta\lambda$  and limited to the high-frequency range, which is irrelevant for the given application.

### 3.5. Python interface

Although *Nektar++* is designed to provide a modern C++ interface to high-order methods, its use of complex hierarchies of classes and inheritance, as well as the fairly complex syntax of C++ itself, can lead to a significant barrier to entry for new users of the code. At the same time, the use of Python in general scientific computing applications, and data science application areas in particular, is continuing to grow, in part due to its relatively simple syntax and ease of use. Additionally, the wider Python community offers a multitude of packages and modules to end users, making it an ideal language through which disparate software can be 'glued' to perform very complex tasks with relative ease. For the purposes of scientific computing codes, the Python C API also enables the use of higher-performance compiled code, making it suitable in instances where interpreted pure Python would be inefficient and impractical, as can be seen in packages such as NumPy and SciPy. These factors therefore make Python an ideal language through which to both introduce new users to a complex piece of software, interact with other software packages and, at the same time, retain a certain degree of performance that would not be possible from a purely interpreted perspective.

The version 5.0 release of *Nektar++* offers a set of high-level bindings for a number of classes within the core *Nektar++* libraries. The purpose of these bindings is to significantly simplify the interfaces to key *Nektar++* libraries, offering both a teaching aid for new users to the code, as well as a way to connect with other software packages and expand the scope of the overall software. To achieve this, we leverage the Boost.Python package [53], which offers a route to handling many of the complexities and subtleties of translating C++ functions and classes across to the Python C API. A perceived drawback of this approach is the lack of automation. As Boost.Python is essentially a wrapper around the Python C API, any bindings must be handwritten, whereas other software such as f2py [54] or SWIG [55] offer the ability to automatically generate bindings from the C++ source. However, our experience of this process has been that, other than implementation effort,

handwritten wrappers provide higher quality and more stability, particularly when combined with an automated continuous integration process as is adopted in *Nektar++*, as well as better interoperability with key Python packages such as numpy. In our particular case, heavy use of C++11 features such as `shared_ptr` and the *Nektar++* `Array` class for shared storage meant that many automated solutions would not be well-suited to this particular application.

An example of the Python bindings can be seen in Listing 1, where we perform the Galerkin projection of the smooth function  $f(x, y) = \cos(x)\cos(y)$  onto a standard quadrilateral expansion at order  $P = 7$ , using  $P+1$  Gauss-Lobatto-Legendre quadrature points to exactly integrate the mass matrix. We additionally perform an integral of this function (whose exact value is  $4\sin^2(1)$ ). As can be seen in this example, the aim of the bindings is to closely mimic the layout and structure of the C++ interface, so that they can be used as a learning aid for to the full C++ API. Additionally, the Python bindings make full use of Boost.Python's automatic datatype conversion facilities. In particular, significant effort has been extended to facilitate seamless interaction between the NumPy `ndarray` class, which is almost universally used in Python scientific computing applications for data storage, and the *Nektar++* storage `Array<OneD, *>` classes. This allows an `ndarray` to be passed into *Nektar++* functions directly and vice versa. Moreover this interaction uses the Boost.Python interface to NumPy to ensure that instead of copying data (which could be rather inefficient for large arrays), this interaction uses a shared memory space between the two data structures. Reference counting is then used to ensure data persistence and memory deallocation, depending on whether memory was first allocated within the C++ environment or Python.

Listing 1: Using the *Nektar++* 5.0 Python bindings to perform a simple Galerkin projection and integral on a standard quadrilateral element.

---

```
import NekPy.LibUtilities as LibUtil
import NekPy.StdRegions as StdReg
import numpy as np

# Set P = 8 modes and Q = P + 1 quadrature points.
nModes = 8
nPts = nModes + 1

# Create GLL-distributed quadrature points.
pType = LibUtil.PointsType.GaussLobattoLegendre
pKey = LibUtil.PointsKey(nPts, pType)

# Create modified C^0 basis on these points.
bType = LibUtil.BasisType.Modified_A
bKey = LibUtil.BasisKey(bType, nModes, pKey)

# Create quadrilateral expansion using this basis
# in each coordinate direction (tensor product).
quad = StdReg.StdQuadExp(bKey, bKey)

# L^2 projection of f(x,y) = cos(x)*cos(y) onto the
# quadrilateral element. Note x,y are numpy ndarrays
# and evaluation of cos() is performed using numpy.
x, y = quad.GetCoords()
fx = np.cos(x) * np.cos(y)
proj = quad.FwdTrans(fx)

# Integrate function over the element.
print("Integral = {:.4f}".format(quad.Integral(fx)))
```

---

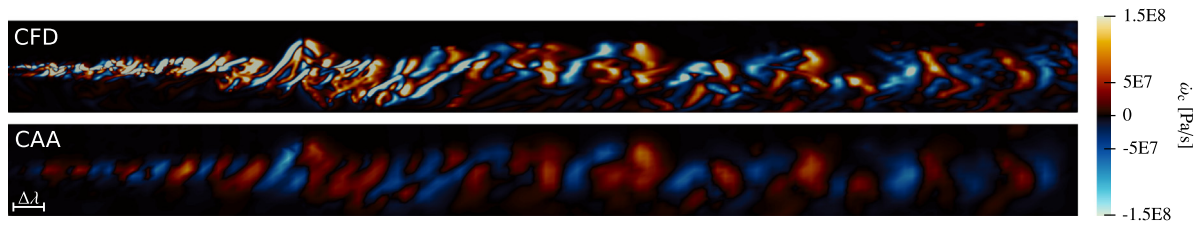


**Fig. 3.** Instantaneous acoustic source term as represented in CFD (proprietary finite volume flow solver with  $\Delta h < 1.4$  mm mesh) and CAA (*Nektar++* AcousticSolver with  $\Delta h = 20$  mm mesh and fourth order expansion). Slice through a three-dimensional domain.

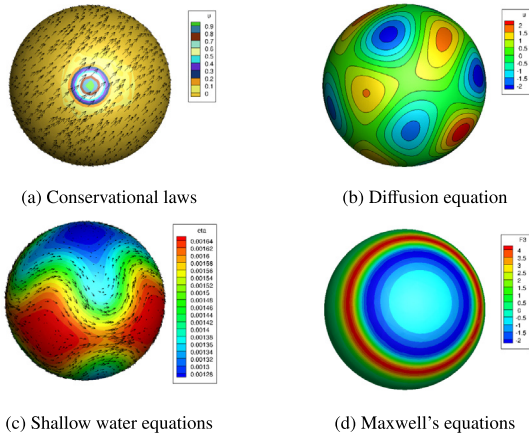


**Fig. 4.** Numerical simulation of the MMF scheme in *Nektar++* for several partial differential equations solved on the sphere.

#### 4. Developments in numerical methods

This section highlights our recent developments on numerical methods contained within the *Nektar++* release.

##### 4.1. Method of moving frames

Modern scientific computation faces unprecedented demands on computational simulation in multidimensional complex domains composed of various materials. Examples of this include solving shallow water equations on a rotating sphere for weather prediction, incorporating biological anisotropic properties of cardiac and neural tissue for clinical diagnosis, and simulating the electromagnetic wave propagation on metamaterials for controlling electromagnetic nonlinear phenomena. All of these examples require the ability to solve PDEs on manifolds embedded in higher-dimensional domains. The method of moving frames (MMF) implemented in *Nektar++* is a novel numerical scheme for solving such computational simulations in geometrically-complex domains.

Moving frames, principally developed by Élie Cartan in the context of Lie groups in the early 20th century [56–58], are orthonormal vector bases that are constructed at every grid point in the discrete space of a domain  $\Omega$ . Moving frames are considered as an ‘independent’ coordinate system at each grid point, and can be viewed as a dimensional reduction because the number of moving frames corresponds to dimensionality, independent of the space dimension. In this sense, ‘moving’ does not mean that the frames are time-dependent, but are different in a pointwise sense: i.e. if a particle travels from one point to the other, then it may undergo a different frame, which looks like a series of ‘moving’ frames. More recently this approach has been adapted more practical and computational purposes, mostly in computer vision [59–61] and medical sciences [62].

Building such moving frames is easily achieved by differentiating the parametric mapping  $\mathbf{x}$  of a domain element  $\Omega_e$  with respect to each coordinate axis of a standard reference space, followed by a Gram–Schmidt orthogonalisation process. We obtain orthonormal vector bases, denoted as  $\mathbf{e}^i$ , with the following properties:

$$\mathbf{e}^i \cdot \mathbf{e}^j = \delta_{ij}, \quad \|\mathbf{e}^i\| = 1, \quad 1 \leq i, j \leq 3,$$

where  $\delta_{ij}$  denotes the Kronecker delta. Moreover, the moving frames are constructed such that they are differentiable within each element and always lie on the tangent plane at each grid point. These two intrinsic properties of frames implies that any vector or the gradient can be expanded on moving frames as follows:

$$\mathbf{v} = v^1 \mathbf{e}^1 + v^2 \mathbf{e}^2, \quad \nabla u = u^1 \mathbf{e}^1 + u^2 \mathbf{e}^2.$$

Applying this expansion to a given PDE enables us to re-express it with moving frames on any curved surface. Then, the weak formulation of the PDE with moving frames, called the *MMF scheme*, on a curved surface is similar to the scheme in the Euclidean space, in the sense that it contains no metric tensor or its derivatives and it does not require the construction of a continuous curved axis in  $\Omega$  which often produces geometric singularities. This is a direct result of the fact that moving frames are *locally* Euclidean. However, the numerical scheme with moving frames results in the accurate solutions of PDEs on any types of surfaces such as spheres, irregular surfaces, or non-convex surfaces. Some examples of simulations that can be achieved under this approach include conservation laws [63], the diffusion equation [64], shallow water equations (SWEs) [65], and Maxwell’s equations [66]. Representative results from *Nektar++* for these equations on the surface of a sphere are shown in Fig. 4.

Moreover, moving frames have been proven to be efficient for other geometrical realisations, such as the representation of anisotropic properties of media on complex domains [64], incorporating the rotational effect of any arbitrary shape [65], and adapting isotropic upwind numerical flux in anisotropic media [66]. The accuracy of the MMF scheme with the higher-order curvilinear meshes produced by *NekMesh*, described in Section 5.1, is reported to be significantly improved for a high  $p$  and conservational properties such as mass and energy after a long time integration, whereas the accuracy of the MMF-SWE scheme on *NekMesh* is presented to be the best among all the previous SWE numerical schemes [67]. Ongoing research topics on moving frames are to construct the connections of frames, to compute propagational curvature, and finally to build an *Atlas* (a geometric map with connection and curvature) in order to provide a quantitative measurement and analysis of a flow on complex geometry. Examples of ongoing research topics in this area include electrical activation in the heart [68] and fibre tracking of white matter in the brain.

##### 4.2. Spatially-variable polynomial order

An important difficulty in the simulation of flows of practical interest is the wide range of length- and time-scales involved, especially in the presence of turbulence. This problem is aggravated

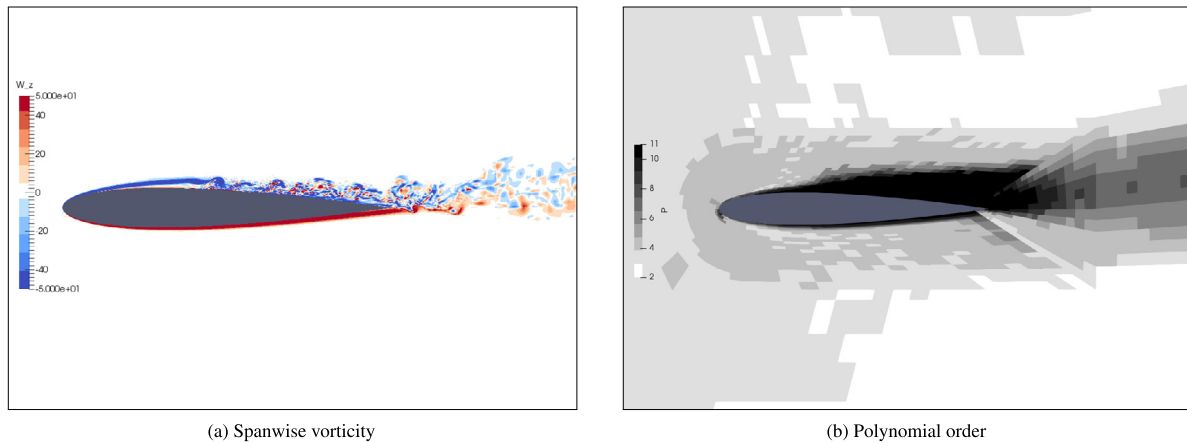


**Fig. 5.** Polynomial order and vorticity distributions obtained with simulation using adaptive polynomial order for the flow around a NACA 0012 profile with  $Re = 50,000$  and  $\alpha = 6^\circ$ .  
Source: Taken from [69].

by the fact that in many cases it is difficult to predict where in the domain an increase in the spatial resolution is required before conducting the simulation, while performing a uniform refinement across the domain is computationally prohibitive. Therefore, in dealing with these types of flows, it is advantageous to have an adaptive approach which allows us to dynamically adjust the spatial resolution of the discretisation both in time and in space.

Within the spectral/ $hp$  element framework, it is possible to refine the solution following two different routes.  $h$ -refinement consists of reducing the size of the elements as would be done in low-order methods. This is the common approach for the initial distribution of degrees of freedom over the domain, with the computational mesh clustering more elements in regions where small scales are expected to occur, such as boundary layers. The other route is  $p$ -refinement (sometimes called  $p$ -enrichment), where the spatial resolution is increased by using a higher polynomial order to represent the solution. As discussed in [69], the polynomial order can be easily varied across elements in the spectral/ $hp$  element method if the expansion basis is chosen appropriately. In particular if a basis admits a boundary–interior decomposition, such as the modified  $C^0$  basis described in Section 2 or the classical Lagrange interpolant basis, then the variation in polynomial order can be built into the assembly operation between interconnected elements. This allows for a simple approach to performing local refinement of the solution, requiring only the adjustment of the polynomial order in each element.

With this in mind, an adaptive polynomial order procedure has been implemented in *Nektar++*, with successful applications to simulations of incompressible flows. The basic idea in this approach is to adjust the polynomial order during the solution based on an element-local error indicator. The approach we used is similar to that demonstrated for shock capturing in [70], whereby oscillatory behaviour in the solution field is detected by an error sensor on each element  $\Omega_e$  calculated as

$$S_e = \frac{\|u_p - u_{p-1}\|_2^2}{\|u_p\|_2^2},$$

where  $u_p$  is the solution obtained for the  $u$  velocity using the current polynomial order  $P$ ,  $u_{p-1}$  is the projection of this solution to a polynomial of order  $P - 1$  and  $\|\cdot\|_2$  denotes the  $L^2$  norm. After each  $n_{\text{steps}}$  time-steps, this estimate is evaluated for each element. For elements where the estimate of the error is above a chosen threshold,  $P$  is incremented by one, whereas in elements with low error  $P$  is decremented by one, respecting minimum and maximum values for  $P$ . The choice of  $n_{\text{steps}}$  is critical for the

efficiency of this scheme, since it has to be sufficiently large to compensate for the costs of performing the refinement over a large number of time-steps, yet small enough to adjust to changes in the flow. More details on this adaptive procedure for adjusting the polynomial order, as well as its implementation in both CG and DG regimes, are found in [69].

An example of an application of the adaptive polynomial order procedure is presented in Fig. 5, showing the spanwise vorticity and polynomial order distributions for a quasi-3D simulation of the incompressible flow around a NACA 0012 profile at Reynolds number  $Re = 50,000$  and angle of attack  $\alpha = 6^\circ$ . The session files to generate this data can be found in Example A.17. It is clear that the regions with transition to turbulence and the boundary layers are resolved using the largest polynomial order allowed, while regions far from the aerofoil use a low polynomial order. This way, the scheme succeeds in refining the discretisation in the more critical regions where small scales are present, without incurring in the large computational costs that would be required to uniformly increase the polynomial order. More simply stated, it is possible to specify different polynomial order in the quadrilateral elements (typically used in boundary layer discretisation) and the triangle elements (typically used to fill the outer volume). As a final point, we note that the use of variable polynomial order is not limited to quasi-3D simulations; both CG and DG discretisations fully support all element shape types in 2D and 3D, with parallel implementations (including frequently used preconditioners) also supporting this discretisation option.

#### 4.3. Global mapping

Even though the spectral/ $hp$  element spatial discretisation allows us to model complex geometries, in some cases it can be advantageous to apply a coordinate transformation for solving problems that lie in a coordinate system other than the Cartesian frame of reference. This is typically the case when the transformed domain possesses a symmetry; this allows us to solve the equations more efficiently by compensating for the extra cost of applying the coordinate transformation. Examples of this occur when a transform can be used to map a non-homogeneous geometry to a homogeneous geometry in one or more directions. This makes it possible to use the cheaper quasi-3D approach, where this direction is discretised using a Fourier expansion, and also for problems with moving boundaries, where we can map the true domain to a fixed computational domain, avoiding the need for recomputing the system matrices after every time-step.



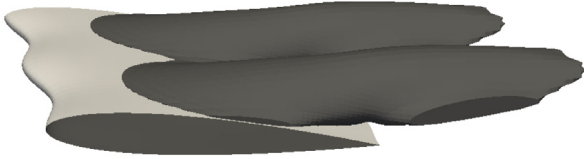


Fig. 6. Time-averaged streamwise reversing regions for incompressible flow over a wing with spanwise waviness with  $Re = 1000$  and  $\alpha = 12^\circ$ .

The implementation of this method was achieved in two parts. First, a new library called `GlobalMapping` was created, implementing general tensor calculus operations for several types of transformations. Even though it would be sufficient to consider just a completely general transformation, specific implementations for particular cases of simpler transformations are also included in order to improve the computational efficiency, since in these simpler cases many of the metric terms are trivial. In a second stage, the incompressible Navier–Stokes solver was extended, using the functionality of the `GlobalMapping` library to implement the methods presented in [71]. Some examples of applications are given in [72,73]. Embedding these global mappings at the library level allows similar techniques to be introduced in other solvers in the future.

Fig. 6 presents an example of the application of this technique, indicating the recirculation regions (i.e. regions where the streamwise velocity is negative) for the flow over a wing with spanwise waviness. In this case, the coordinate transformation removes the waviness from the wing, allowing us to treat the transformed geometry with the quasi-3D formulation. It is important to note that this technique becomes unstable as the waviness amplitude becomes too large. The fully explicit mapping is more sensitive to instability than the semi-implicit mapping as discussed in [71]. However, in cases where it can be successfully applied, it leads to significant gains in terms of computational cost when compared against a fully 3D implementation. The session files used in this example can be found in Example A.18.

## 5. Applications

In this section, we demonstrate some of the new features provided in our new release, with a focus on application areas.

### 5.1. NekMesh

In the previous publication [33], we briefly outlined the `MeshConvert` utility, which was designed to read various external file formats and perform basic processing and format conversion. In the new release of `Nektar++`, `MeshConvert` has been transformed into a new application, called `NekMesh`, which provides a series of tools for both the generation of meshes from an underlying CAD geometry, as well as the manipulation of linear meshes to make them suitable for high-order simulations. While `MeshConvert` was dedicated to the conversion of external mesh file formats, the scope of `NekMesh` has been significantly broadened to become a true stand-alone high-order mesh generator.

The generation of high-order meshes in `NekMesh` follows an *a posteriori* approach proposed in [74]. We first generate a linear mesh using traditional low-order mesh generation techniques. We then add additional nodes along edges, faces and volumes to achieve a high-order polynomial discretisation of our mesh. In the text below, we refer to these additional nodes as ‘high-order’ nodes, as they do not change the topology of the underlying linear mesh, but instead deform it to fit a required geometry. In this bottom-up procedure, these nodes are first added on edges,

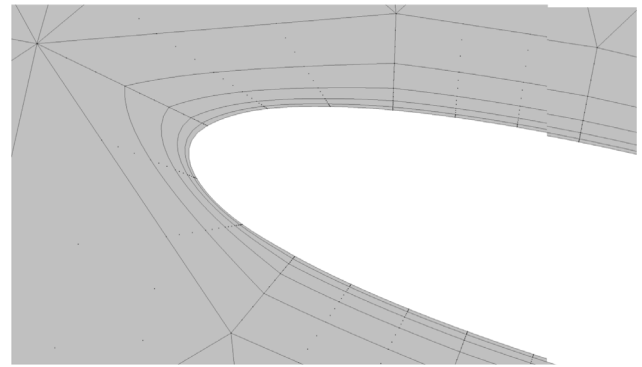


Fig. 7. Example of split boundary layer mesh.

followed by faces and finally the volume-interior. At each step, nodes are generated on boundaries to ensure a geometrically accurate representation of the model.

A key issue in this process, however, is ensuring that elements remain valid after the insertion of high-order nodes, as this process is highly sensitive to boundary curvature. A common example of this is in boundary layer mesh generation [75], where elements are typically extremely thin in order to resolve the high-shear of the flow near the wall. In this setting, naively introducing curvature into the element will commonly push one face of the element through another, leading a self-intersecting element and thus a mesh that is invalid for computation.

An important contribution of `NekMesh` to the high-order mesh generation community was presented in [75,76], where we alleviate this risk through the creation of a coarse, single element boundary layer mesh with edges orthogonal to the boundary. The thickness of the layer of elements gives enough room for a valid curving of the ‘macro’-elements. After creation of the high-order mesh, a splitting of these boundary elements can be performed using the isoparametric mapping between the reference space and the physical space. We then apply the original isoparametric mapping to construct new elements within the ‘macro’ element, thereby guaranteeing their validity. This ensures conservation of the validity and quality of subdivided elements while achieving very fine meshes. An example is shown in Fig. 7 where the coarse boundary layer mesh of Fig. 8 was split into five layers, using a geometric progression of growth rate  $r = 2$  in the thickness of each layer. The session files used to create the meshes for Figs. 8 and 9 can be found in Example A.20.

A complementary approach to avoid invalid or low quality high-order elements is to optimise the location of high-order nodes in the mesh. The approach proposed in [13,77] of a variational framework for high-order mesh optimisation was implemented in `NekMesh`. In this approach, we consider the mesh to be a solid body, and define a functional based on the deformation of each high-order element. This functional can correspond to physical solid mechanics governing equations such as linear or non-linear elasticity, but also provides the possibility to accommodate arbitrary functional forms such as the Winslow equations within the same framework. Minimising this functional is then achieved through classical quasi-Newton optimisation methods with the use of analytic gradient functions, alongside a Jacobian regularisation technique to accommodate initially-invalid elements. As demonstrated in [13], the approach is scalable and allows the possibility to implement advanced features, such as the ability to slide nodes along a given constrained CAD curve or surface.

Along these lines, much of the development of `NekMesh` has focused on the access to a robust CAD system for CAD queries required for traditional meshing operations. Assuming that the

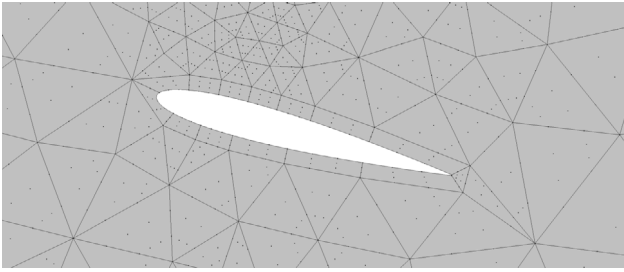


Fig. 8. Example of mesh generated around a NACA 0012 aerofoil.

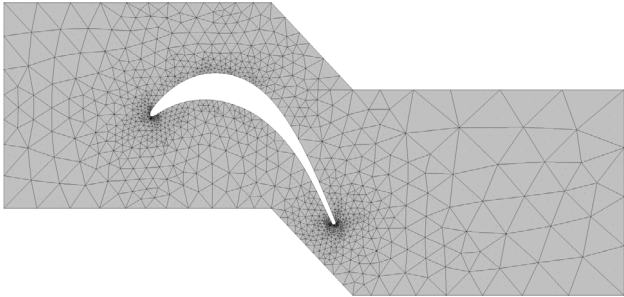


Fig. 9. Example of mesh generated around a t106c turbine blade.

CAD is watertight, we note that only a handful of CAD operations are required for mesh generation purposes. *NekMesh* therefore implements a lightweight wrapper around these CAD queries, allowing it to be interfaced to a number of CAD systems. By default, we provide an interface to the open-source OpenCASCADE library [78]. OpenCASCADE is able to read the STEP CAD file format, natively exported by most CAD design tools, and load it into the system. At the same time, the use of a wrapper means that users and developers of *NekMesh* are not exposed to the extensive OpenCASCADE API. Although OpenCASCADE is freely available and very well suited to simple geometries, it lacks many of the CAD healing tools required for more complex geometries of the type typically found in industrial CFD environments, which can frequently contain many imperfections and inconsistencies. However, the use of a lightweight wrapper means that other commercial CAD packages can be interfaced to *NekMesh* if available. To this end, we have implemented a second CAD interface to the commercial CFI CAD engine, which provides a highly robust interface and is described further in [39,77,79].

While users are recommended to create their CAD models in a dedicated CAD software, export them in STEP format and load them in *NekMesh*, they also have the possibility to create their own simple two-dimensional models using one of two tools made available to them. The first tool is an automatic NACA aerofoil generator. With just three inputs – a NACA code, an angle of attack and dimensions of the bounding box – a geometry is generated and passed to the meshing software. An example is shown in Fig. 8 of a mesh generated around a NACA 0012 aerofoil at an angle of attack of  $\alpha = 15^\circ$ .

The other tool is based on the GEO geometry file format of the Gmsh [80] open source mesh generator. The GEO format is an interpreter for the procedural generation of geometries. *NekMesh* has been made capable to understand basic GEO commands, which gives the possibility to generate simple two-dimensional geometries. An example is shown in Fig. 9 of a mesh generated around a T106C turbine blade: the geometry was created using a GEO script of lines and splines.

## 5.2. Acoustic solver

Time-domain computational aeroacoustics simulations are commonly used to model noise emission over wide frequency ranges or to augment flow simulations in hybrid setups. Compared with fully compressible flow simulations, they require less computational effort due to the reduced complexity of the governing equations and larger length scales [81]. However, due to the small diffusive terms, as well as the long integration times and distances required for these simulations, highly accurate numerical schemes are crucial for stability [82]. This numerical accuracy can be provided by spectral/*hp* element methods, even on unstructured meshes in complex geometries, and hence *Nektar++* provides a good candidate framework on which to build such an application code.

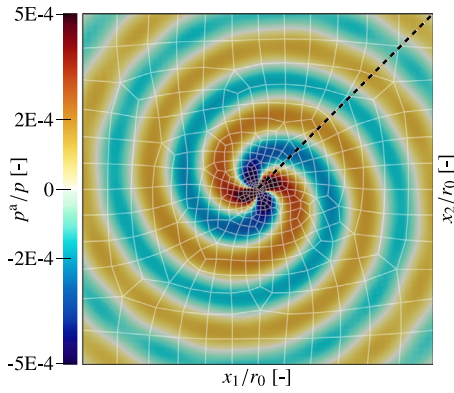
The latest release of *Nektar++* includes a new *AcousticSolver*, which implements several variants of aeroacoustic models. These are formulated in a hyperbolic setting and implemented in a similar fashion to the compressible Euler and Navier–Stokes equations, encapsulated in *Nektar++* inside the *CompressibleFlowSolver*. Following this implementation guideline, the *AcousticSolver* uses a discontinuous Galerkin spatial discretisation with modal or nodal expansions to model time-domain acoustic wave propagation in one, two or three dimensions. It implements the operators of the linearised Euler Equations (LEE) and the Acoustic Perturbation Equations 1 and 4 (APE-1/4) from [83], both of which describe the evolution of perturbations around a base flow state. For the APE-1/4 operator, the system is defined by the hyperbolic equations

$$\frac{\partial p^a}{\partial t} + \bar{c}^2 \nabla \cdot \left( \bar{\rho} \mathbf{u}^a + \bar{\mathbf{u}} \frac{p^a}{c^2} \right) = \dot{\omega}_c, \quad (4a)$$

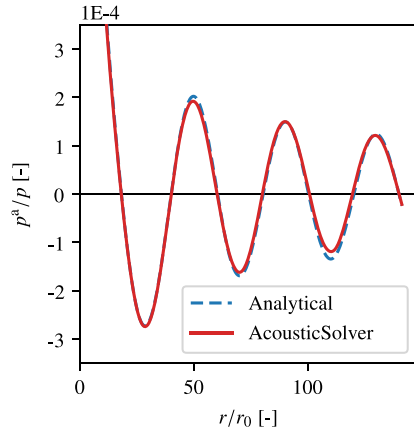
$$\frac{\partial \mathbf{u}^a}{\partial t} + \nabla (\bar{\mathbf{u}} \cdot \mathbf{u}^a) + \nabla \left( \frac{p^a}{\bar{\rho}} \right) = \dot{\omega}_m, \quad (4b)$$

where  $\mathbf{u}$  denotes the flow velocity,  $\rho$  its density,  $p$  its pressure and  $c$  corresponds to the speed of sound. The quantities  $\mathbf{u}^a$  and  $p^a$  refer to the irrotational acoustic perturbation of the flow velocity and its pressure, with overline quantities such as  $\bar{\mathbf{u}}$  denoting the time-averaged mean. The right-hand-side acoustic source terms  $\dot{\omega}_c$  and  $\dot{\omega}_m$  are specified in the session file. This allows for the implementation of any acoustic source term formulation so that, for example, the full APE-1 or APE-4 can be obtained. In addition to using analytical expressions, the source terms and base flow quantities can be read from disk or transferred from coupled applications, enabling co-simulation with a driving flow solver. Both, LEE and APE support non-quietest base flows with inhomogeneous speed of sounds. Accordingly, the Lax–Friedrichs and upwind Riemann solvers used in the *AcousticSolver* employ a formulation which is valid even for strong base flow gradients. The numerical stability can be further improved by optional sponge layers and suitable boundary conditions, such as rigid wall, farfield or white noise.

A recurring test case for APE implementations is the “spinning vortex pair” [84]. It is defined using two opposing vortices, that are each located at  $r_0$  from the centre  $x_1 = x_2 = 0$  of a square domain with edge length  $-100 r_0 \leq x_{1,2} \leq 100 r_0$ . The vortices have a circulation of  $\Gamma$  and rotate around the centre at the angular frequency  $\omega = \Gamma/4\pi r_0^2$  and circumferential Mach number  $Ma_r = \Gamma/4\pi r_0 c$ . The resulting acoustic pressure distribution is shown in Fig. 10a and was obtained on an unstructured mesh of 465 quadrilateral elements with a fifth order modal expansion ( $P = 5$ ). The session files used to generate this example can be found in Example A.19. Along the black dashed line, the acoustic pressure shown in Fig. 10b exhibits minor deviations from the analytical solution defined in [84], but is in excellent agreement with the results of the original simulation in [83]. The latter was based on a structured mesh with 19,881 nodes and employed a



(a) Normalized acoustic pressure distribution at  $t = 1$  s with the mesh shown in light gray and the sampling line in a black dashed line.



(b) Normalized acoustic pressure along sample line, obtained with the AcousticSolver and analytical solution [84].

**Fig. 10.** Normalised acoustic pressure for  $\Gamma/(cr_0) = 1.0$  and  $Ma_r = 0.0795$  at  $t = 1$  s.

sponge layer boundary condition and spatial filtering to improve the stability. Due to the flexibility and numerical accuracy of the spectral/ $hp$  method, a discretisation with only 16,740 degrees of freedom was sufficient for this simulation, and no stabilisation measures (e.g. SVV or filtering) were necessary to reproduce this result.

### 5.3. Fluid–structure interaction (FSI) and vortex-induced vibration (VIV)

Fluid–structure interaction (FSI) modelling poses a great challenge for the accurate prediction of vortex-induced vibration (VIV) of long flexible bodies, as the full resolution of turbulent flow along their whole span requires considerable computational resources. This is particularly true in the case of large aspect-ratio bodies. Although 2D strip-theory-based modelling of such problems is much more computationally efficient, this approach is unable to resolve the effects of turbulent fluctuations on dynamic coupling of FSI systems [85,86]. A novel strip model, which we refer to as ‘thick’ strip modelling, has been developed using the *Nektar++* framework in [87], whose implementation is supported within the incompressible Navier–Stokes solver. In this approach, a three-dimensional DNS model with a local spanwise scale is constructed for each individual strip. Coupling between strips is modelled implicitly through the structural dynamics of the flexible body.

In the ‘thick’ strip model, the flow dynamics are governed by a series of incompressible Navier–Stokes equations. The governing

equations over a general local domain  $\Omega_n$  associated with the  $n$ th strip are written as

$$\frac{\partial \mathbf{u}_n}{\partial t} + (\mathbf{u}_n \cdot \nabla) \mathbf{u}_n = -\nabla p_n + \frac{1}{Re} \nabla^2 \mathbf{u}_n \quad \text{on } \Omega_n \quad (5)$$

$$\nabla \cdot \mathbf{u}_n = 0 \quad \text{on } \Omega_n, \quad (6)$$

where the vector  $\mathbf{u}_n = (u_n, v_n, w_n)$  denotes the fluid velocity inside the  $n$ th strip, with  $p_n$  being the corresponding dynamic pressure and  $Re$  the Reynolds number, which we assume to be constant across all strips. The governing equations are supplemented by boundary conditions of either Dirichlet or Neumann type. In particular, no-slip boundary conditions are applied to the wall of the body, and the velocity of the moving wall is imposed and determined from the transient solution of structural dynamics equations of motion. A linearised tensioned beam model is used to describe the structural dynamic behaviour of the flexible body, which is expressed by the system

$$\rho_c \frac{\partial^2 \boldsymbol{\eta}}{\partial t^2} + c \frac{\partial \boldsymbol{\eta}}{\partial t} - T \frac{\partial^2 \boldsymbol{\eta}}{\partial z^2} + EI \frac{\partial^4 \boldsymbol{\eta}}{\partial z^4} = \mathbf{f}. \quad (7)$$

In the above,  $\rho_c$  is the structural mass per unit length,  $c$  is the structural damping per unit length,  $T$  is the tension and  $EI$  is the flexural rigidity.  $\mathbf{f}$  denotes the vector of hydrodynamic force per unit length exerted on the body’s wall and  $\boldsymbol{\eta}$  is the structural displacement vector.

Homogeneity is imposed in the spanwise direction to the local flow within individual strips, under the assumption that the width of the strips is much shorter with respect to the oscillation wavelength of excited higher-order modes of the flexible body. This therefore enables the use of the computationally-efficient quasi-3D approach discussed in previous sections within each strip domain, in which two-dimensional spectral elements with piecewise polynomial expansions are used in the  $(x, y)$  plane and Fourier expansions are used in the homogeneous  $z$  direction. This also requires the assumption of a spanwise oscillation of the flexible body with respect to its full-length scale. As a consequence, the motion variables and fluid forces are expressed as a complex Fourier series, and the tensioned beam model is decoupled into a set of ordinary differential equations, which can be solved simply by a second-order Newmark- $\beta$  method [88]. A partitioned approach is adopted to solve the coupled FSI system, in which coordinate mapping technique discussed in Section 4.3 is implemented for the treatment of the moving wall [71].

To illustrate the application of this modelling approach, VIV of a long flexible cylinder with an aspect ratio of  $32\pi$  which is pinned at both ends is simulated at  $Re = 3900$ , with 16 thick strips allocated evenly along the axial line of the cylinder. The instantaneous spanwise wake structure is visualised by the vortex-identification of Q-criterion in Fig. 11. As the figure demonstrates, the distribution of vortex shedding illustrates that a second harmonic mode is excited along the spanwise length and the turbulent structure is captured well in the local domain of the strips. This emphasises the convincing advantage of providing highly-resolved description of hydrodynamics involved in the FSI process. The session files used to run this simulation can be found in Example A.21.

### 5.4. Aeronautical applications

CFD is now an indispensable tool for the design of aircraft engines, and it has become commonplace in the design guidance of new technologies and products [89]. In order for CFD to be effectively adopted in industry, validation and verification is required over a broad design space. This is challenging for



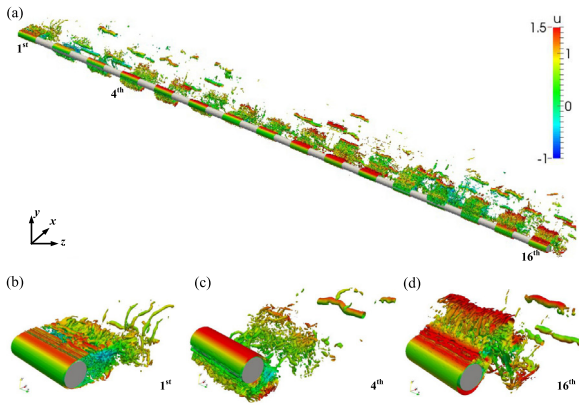


**Fig. 11.** Instantaneous vortex shedding visualised by the vortex-identification of Q-criterion (iso-surfaces of the Q-value =  $[-5, 5]$ ) in body-fitted coordinates: (a) full domain view and zoom-in view of (b) first strip; (c) fourth strip and (d) 16th strip.

a number of reasons, including the range of operating conditions (i.e. Reynolds numbers, Mach numbers, temperatures and pressures), the complexity of industrial geometries (including uncertainty due to manufacturing variations) and their relative motion (i.e. rotor-stator interactions). Even though RANS continues to be the backbone of CFD-based design, the recent development of high-order unstructured solvers and high-order unstructured meshing algorithms, combined with the lowering cost of HPC infrastructures, has the potential to allow for the introduction of high-fidelity transient simulations using large-eddy or direct numerical simulations (LES/DNS) in the design loop, taking the role of a virtual wind tunnel.

As part of our effort to bridge the gap between academia and industry, we have been developing the expertise to analyse turbomachinery cases of industrial interest using *Nektar++*. A key problem to overcome in these cases is the sensitivity of these simulations to variations in spatial resolution, which requires the use of stabilisation techniques in order to improve robustness. *Nektar++* makes use of the spectral vanishing viscosity (SVV) method, originally introduced for the Fourier spectral method by Tadmor [90]. SVV is a model-free stabilisation technique that acts at the subgrid-scale level and allows for exponential convergence properties to be conserved in sufficiently resolved simulations. Recent developments in this area have focused on a new SVV kernel by Moura et al. [3], which replicates the desirable dispersion and diffusion properties of DG schemes and does not require the manual tuning of parameters found in the classical SVV formulation. More specifically, the dissipation curves of the CG scheme of order  $P$  were compared to those of DG order  $P - 2$ , and the DG kernel was determined from minimisation of the pointwise  $L_2$  norm between these curves. SVV stabilisation is combined with spectral/ $hp$  dealiasing [29] to eliminate errors arising from the integration of non-linear terms.

A T106A low pressure turbine vane was investigated at moderate regime ( $Re = 88,450$ ), and the convergence properties of the main flow statistics were extensively explored with the aim of developing a set of best practices for the use of spectral/ $hp$  element methods as a high-fidelity digital twin [91]. The velocity correction scheme of [92] implemented in the *IncNavierStokesSolver* is adopted, using the quasi-3D approach discussed in the previous sections and Taylor-Hood type elements in 2D (where spaces of order  $P$  polynomials on each element are used for the velocity components, and  $P - 1$  for pressure). Uniform inflow velocity is combined with pitchwise periodicity and high-order outflow boundary conditions [93]. Numerical stability is ensured

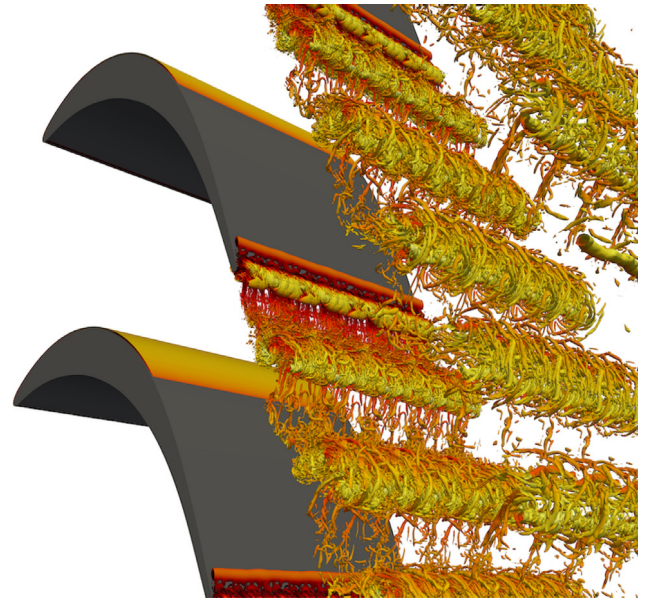


**Fig. 12.** Instantaneous isosurfaces of Q-criterion ( $Q = 500$ ) contoured by velocity magnitude, showing the vortical structures evolving on the suction surface and in the wake of a T106A cascade. The computational domain is replicated in the spanwise and pitchwise directions for visual clarity.

by employing SVV with the DG kernel in the  $x$ - $y$  planes, and the traditional exponential kernel for the spanwise Fourier direction. A representation of the vortical structures is shown in Fig. 12: transition to turbulence takes place only in the final portion of the suction surface, where the separated shear layer rolls up due to Kelvin-Helmholtz instability. The separation bubble remains open and merges into the trailing edge wake, giving rise to large-scale vortical structures. This work was conducted with clean inflow conditions to isolate the effect of the numerical setup on the various flow statistics. However, turbomachinery flows are highly turbulent: subsequent work focused on the treatment of flow disturbances to reproduce more accurately a realistic environment [94]. With this aim, a localised synthetic momentum forcing was introduced in the leading edge region to cause flow symmetry breakdown on the suction surface, and promote anticipated transition to turbulence. This approach yields an improvement in the agreement with experimental data, with no increase in the computational cost.

With the intent of being able to tackle cases in which compressibility effects are not negligible, there has been an effort in validating the *CompressibleFlowSolver* for shock-wave boundary layer interaction (SWBLI) configurations. This solver, described in our previous publication [33], formulates the compressible Navier-Stokes equations in their conservative form, discretised using a DG scheme and explicit time-stepping methods. In order to regularise the solution in the presence of discontinuities, the right hand side of the Navier-Stokes equations is augmented with a Laplacian viscosity term of the form  $\nabla \cdot (\varepsilon \nabla \mathbf{q})$ , where  $\mathbf{q}$  is the vector of conserved variables, and  $\varepsilon$  is a spatially-dependent diffusion term that is defined on each element as

$$\varepsilon = \varepsilon_0 \frac{h}{p} \lambda_{\max} S.$$

Here,  $\varepsilon_0$  is a  $O(1)$  constant,  $\lambda_{\max}$  is the maximum local characteristic speed,  $h$  is a reference length of the element,  $p$  its polynomial order, and  $S$  a discontinuity sensor value using the formulation of [70]. To benchmark this approach in the context of SWBLI

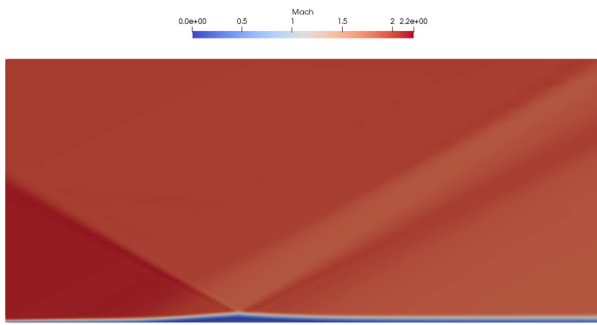


Fig. 13. Mach number field of SWBLI test case ( $60 \times 40$  quadrilateral elements,  $p = 3$ ); configuration based on [95].

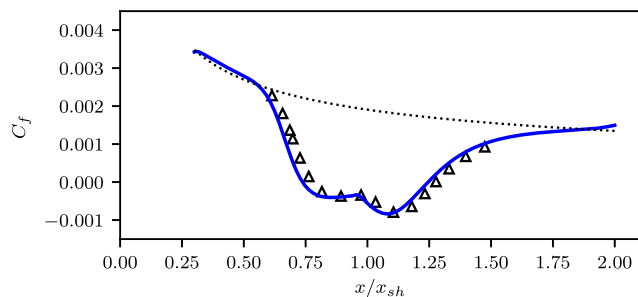


Fig. 14. Skin friction coefficient for the SWBLI test case: blue line *Nektar++* ( $60 \times 40$  quadrilateral elements,  $p = 3$ ); triangles are from [96]; dotted line is empirical solution by [99].

problems, we consider a laminar problem studied experimentally and numerically in [95]. Several authors have studied this SWBLI with slightly different free stream conditions; here we follow the physical parameters used by [96], where we select a free-stream Mach number  $Ma = 2.15$ , shock angle  $\beta = 30.8^\circ$ , a stagnation pressure  $p_0 = 1.07 \times 10^4$  Pa, a stagnation temperature of  $T_0 = 293$  K, a Reynolds number  $Re = 10^5$  (referred to the inviscid shock impingement location  $x_{sh}$  measured from the plate leading edge), and a Prandtl number  $Pr = 0.72$ . Unlike [96], the leading edge is not included in the simulations. The inflow boundary is located at  $x = 0.3x_{sh}$  where the analytical compressible boundary layer solution of [97] is imposed. The session files used in this example can be found in Example A.22. At the inlet, the Rankine–Hugoniot relations that describe the incident shock are superimposed over the compressible boundary layer solution. At the top boundary we impose the constant states corresponding to inviscid post incident shock wave state. At the outlet in the subsonic part of the boundary layer a pressure outlet is imposed based on the inviscid post reflected state conditions. All boundary conditions are imposed in a weak sense through a Riemann solver, as described in [98], and use a coarse grid of  $60 \times 40$  quadrilateral elements at order  $p = 3$ . For illustrative purposes, Fig. 13 shows a snapshot of the Mach number field. For a more quantitative comparison, Fig. 14 compares the skin friction coefficient with those from [99] and [96], which is in fair agreement with the results of [96].

## 6. Availability

*Nektar++* is open-source software, released under the MIT license, and is freely available from the project website (<https://www.nektar.info/>). The git repository is freely accessible and can be found at <https://gitlab.nektar.info/>. Discrete releases are made at milestones in the project and are available to download as compressed tar archives, or as binary packages for a range of operating systems. These releases are considered to contain relatively

complete functionality compared to the repository master branch. Docker container images are also available for these releases and the latest build of master, as well as a Jupyter notebook that contains the Python interface of Section 3.5. These can be found on Docker Hub under the repositories *nektarpp/nektar* and *nektarpp/nektar-workbook* respectively.

## 7. Conclusions

In this paper, we have reviewed the latest features and enhancements of the *Nektar++* version 5.0 release. A key theme of our work in this release has been to evolve the fundamental design of the software detailed in our previous publication [33], towards providing an enabling tool for efficient high-fidelity simulations in various scientific areas. To this end, this latest version of *Nektar++* provides a complete pipeline of tools: from pre-processing with *NekMesh* and a new parallel I/O interface for mesh and field representations; new solvers and improvements to existing ones through numerical developments such as spatially variable polynomial order and the global mapping technique; to parallel post-processing and in-situ processing with the *FieldConvert* utility developments. This gives scientific end-users a tool to enable efficient high-fidelity simulations in a number of fields, such as the applications we discuss in Section 5.

Although this version represents a major milestone in the development of *Nektar++*, there is still clear scope for future work. A particular area of focus remains the efficient use of many-core CPU and GPU systems, recognising that optimisation and performance on an increasingly diverse range of hardware presents a major challenge. Initial research in this area has investigated the use of matrix-free methods as a potential route towards fully utilising computational hardware even on unstructured grids, by combining efficient sum factorisation techniques and the tensor-product basis for unstructured elements presented in [36]. From the perspective of code maintainability, we have also investigated various performance-portable programming models in the context of mesh generation [100] and implicit solvers [101]. Looking towards the next major release of *Nektar++*, we envision the use of these studies as a guideline to implementing efficient operators for the spectral/*hp* element method, whilst retaining ease of use for the development of increasingly efficient solvers.

## Declaration of competing interest

The authors declare that they have no known competing financial interests or personal relationships that could have appeared to influence the work reported in this paper.

## CRediT authorship contribution statement

**David Moxey:** Conceptualization, Methodology, Software, Writing - original draft, Supervision, Funding acquisition. **Chris D. Cantwell:** Conceptualization, Methodology, Software, Validation, Writing - review & editing, Supervision, Funding acquisition. **Yan Bao:** Methodology, Software, Validation, Visualization, Writing - original draft. **Andrea Cassinelli:** Investigation, Software, Validation, Visualization, Writing - original draft. **Giacomo Castiglioni:** Methodology, Software, Validation, Visualization, Writing - original draft. **Sehun Chun:** Software, Methodology, Investigation, Supervision. **Emilia Juda:** Software. **Ehsan Kazemi:** Software. **Kilian Lackhove:** Methodology, Software, Validation, Visualization, Writing - original draft. **Julian Marcon:** Methodology, Software, Validation, Visualization, Writing - original draft. **Gianmarco Mengaldo:** Software, Writing - review & editing. **Douglas Serson:** Methodology, Software, Writing - original draft. **Michael Turner:** Software, Validation. **Hui Xu:** Investigation, Validation. **Joaquim**

**Peiró:** Conceptualization, Writing - review & editing, Supervision, Funding acquisition. **Robert M. Kirby:** Conceptualization, Writing - review & editing, Supervision, Funding acquisition. **Spencer J. Sherwin:** Conceptualization, Software, Writing - review & editing, Supervision, Funding acquisition.

## Acknowledgments

The development of *Nektar++* has been supported by a number of funding agencies including the Engineering and Physical Sciences Research Council (grants EP/R029423/1, EP/R029326/1 EP/L000407/1, EP/K037536/1, EP/K038788/1, EP/L000261/1, EP/I037946/1, EP/H000208/1, EP/I030239/1, EP/H050507/1, EP/D044073/1, EP/C539834/1), the British Heart Foundation (grants FS/11/22/28745 and RG/10/11/28457), the Royal Society of Engineering, European Union FP7 and Horizon 2020 programmes (grant nos. 265780, 671571 and 675008), McLaren Racing, the National Science Foundation (IIS-0914564, IIS-1212806 and DMS-1521748), the Army Research Office (W911NF-15-1-0222), the Air Force Office of Scientific Research and the Department of Energy. HX acknowledges support from the NSFC Grants 91852106 and 91841303. SC acknowledges the support of the National Research Foundation of Korea (No. 2016R1D1A1A02937255). KL acknowledges the Seventh Framework Programme FP7 Grant No. 312444 and German Research Foundation (DFG) Grant No. JA 544/37-2.

## Appendix A. Supplementary data

Supplementary material related to this article can be found online at <https://doi.org/10.1016/j.cpc.2019.107110>.

## References

- R.C. Moura, G. Mengaldo, J. Peiró, S. Sherwin, *J. Comput. Phys.* 330 (2017) 615–623.
- R.C. Moura, G. Mengaldo, J. Peiró, S.J. Sherwin, *Spectral and High Order Methods for Partial Differential Equations ICOSAHOME 2016*, Springer, 2017, pp. 161–173.
- G. Mengaldo, R. Moura, B. Giralda, J. Peiró, S. Sherwin, *Comput. & Fluids* 169 (2018) 349–364.
- G. Mengaldo, D. De Grazia, R.C. Moura, S.J. Sherwin, *J. Comput. Phys.* 358 (2018) 1–20.
- P. Fernandez, R.C. Moura, G. Mengaldo, J. Peraire, *Comput. Methods Appl. Mech. Engrg.* 346 (2019) 43–62.
- P.E. Vos, S.J. Sherwin, R.M. Kirby, *J. Comput. Phys.* 229 (13) (2010) 5161–5181.
- C.D. Cantwell, S.J. Sherwin, R.M. Kirby, P.H.J. Kelly, *Comput. & Fluids* 43 (2011) 23–28.
- C.D. Cantwell, S.J. Sherwin, R.M. Kirby, P.H.J. Kelly, *Math. Mod. Nat. Phenom.* 6 (2011) 84–96.
- G.J. Gassner, *SIAM J. Sci. Comput.* 35 (3) (2013) A1233–A1253.
- G. Mengaldo, D. De Grazia, P.E. Vincent, S.J. Sherwin, *J. Sci. Comput.* 67 (3) (2016) 1272–1292.
- G. Mengaldo, *Discontinuous Spectral/hp Element Methods: Development, Analysis and Applications to Compressible Flows* (Ph.D. dissertation), Imperial College London, 2015.
- G.E. Karniadakis, S.J. Sherwin, *Spectral/hp Element Methods for CFD*, Oxford University Press, 2005.
- M. Turner, J. Peiró, D. Moxey, *Comput. Aided Des.* 103 (2018) 73–91.
- P. Fischer, J. Kruse, J. Mullen, H. Tufo, J. Lottes, S. Kerkemeier, *NEK5000—open source spectral element CFD solver*, Argonne National Laboratory, Mathematics and Computer Science Division, Argonne, IL, see <https://nek5000.mcs.anl.gov/index.php/MainPage>, 2008.
- H.M. Blackburn, S. Sherwin, *J. Comput. Phys.* 197 (2) (2004) 759–778.
- H.M. Blackburn, D. Lee, T. Albrecht, J. Singh, *Comput. Phys. Comm.* 245 (2019) 106804.
- W. Bangerth, R. Hartmann, G. Kanschat, *ACM Trans. Math. Softw. (TOMS)* 33 (4) (2007) 24.
- F. Hindenlang, G.J. Gassner, C. Altmann, A. Beck, M. Staudenmaier, C.-D. Munz, *Comput. & Fluids* 61 (2012) 86–93.
- F.J. Gassner, A.R. Winters, D.A. Kopriva, *J. Comput. Phys.* 327 (2016) 39–66.
- G.X. Giraldo, M. Restelli, *J. Comput. Phys.* 227 (8) (2008) 3849–3877.
- D.S. Abdi, F.X. Giraldo, *J. Comput. Phys.* 320 (2016) 46–68.
- F. Witherden, A. Farrington, P. Vincent, *Comput. Phys. Comm.* 185 (2014) 3028–3040, <http://dx.doi.org/10.1016/j.cpc.2014.07.011>.
- H.T. Huynh, 18th AIAA Computational Fluid Dynamics Conference, 2007, p. 4079.
- Y. Allaneau, A. Jameson, *Comput. Methods Appl. Mech. Engrg.* 200 (49–52) (2011) 3628–3636.
- A. Dedner, R. Klöforn, M. Nolte, M. Ohlberger, *Computing* 90 (3–4) (2010) 165–196.
- A. Bolis, C.D. Cantwell, D. Moxey, D. Serson, S. Sherwin, *Comput. Phys. Comm.* 206 (2016) 17–25.
- P.E. Vos, C. Eskilsson, A. Bolis, S. Chun, R.M. Kirby, S.J. Sherwin, *Int. J. Comput. Fluid Dyn.* 25 (3) (2011) 107–125.
- C.D. Cantwell, S. Yakovlev, R.M. Kirby, N.S. Peters, S.J. Sherwin, *J. Comput. Phys.* 257 (2014) 813–829.
- G. Mengaldo, D. De Grazia, D. Moxey, P.E. Vincent, S. Sherwin, *J. Comput. Phys.* 299 (2015) 56–81.
- A.R. Winters, R.C. Moura, G. Mengaldo, G.J. Gassner, S. Walch, J. Peiro, S.J. Sherwin, *J. Comput. Phys.* 372 (2018) 1–21.
- R.M. Kirby, S.J. Sherwin, *Comput. Methods Appl. Mech. Engrg.* 195 (23–24) (2006) 3128–3144.
- J.-E.W. Lombard, D. Moxey, S.J. Sherwin, J.F. Hoessler, S. Dhandapani, M.J. Taylor, *AIAA J.* 54 (2) (2015) 506–518.
- C.D. Cantwell, D. Moxey, A. Comerford, A. Bolis, G. Rocco, G. Mengaldo, D. de Grazia, S. Yakovlev, J.-E. Lombard, D. Ekelschot, B. Jordi, H. Xu, Y. Mohamied, C. Eskilsson, B. Nelson, P. Vos, C. Biotto, R.M. Kirby, S.J. Sherwin, *Comput. Phys. Comm.* 192 (2015) 205–219, <http://dx.doi.org/10.1016/j.cpc.2015.02.008>.
- H. Xu, C.D. Cantwell, C. Monteserin, C. Eskilsson, A.P. Engsig-Karup, S.J. Sherwin, *J. Hydrodyn.* 30 (1) (2018) 1–22.
- M. Dubiner, *J. Sci. Comput.* 6 (4) (1991) 345–390.
- S.J. Sherwin, G.E. Karniadakis, *Comput. Methods Appl. Mech. Engrg.* 123 (1–4) (1995) 189–229.
- M.G. Duffy, *SIAM J. Numer. Anal.* 19 (6) (1982) 1260–1262.
- F. Bassi, S. Rebay, *J. Comput. Phys.* 138 (2) (1997) 251–285.
- J. Marcon, J. Peiró, D. Moxey, N. Bergemann, H. Bucklow, M. Gammon, *AIAA Scitech 2019 Forum*, American Institute of Aeronautics and Astronautics, Reston, Virginia, 2019, p. 1725, <http://dx.doi.org/10.2514/6.2019-1725>.
- D. Moxey, C.D. Cantwell, R.M. Kirby, S.J. Sherwin, *Comput. Methods Appl. Mech. Engrg.* 310 (2016) 628–645, <http://dx.doi.org/10.1016/j.cma.2016.07.001>.
- D. Moxey, R. Amici, R.M. Kirby, *SIAM J. Sci. Comput.* (2019) submitted for publication.
- S. Yakovlev, D. Moxey, S.J. Sherwin, R.M. Kirby, *J. Sci. Comput.* 67 (1) (2016) 192–220.
- B. Cockburn, C.-W. Shu, *SIAM J. Numer. Anal.* 35 (6) (1998) 2440–2463.
- M. Folk, G. Heber, Q. Koziol, E. Pourmal, D. Robinson, *Proceedings of the EDBT/ICDT 2011 Workshop on Array Databases*, ACM, 2011, pp. 36–47.
- M. Bareford, N. Johnson, M. Weiland, *Improving Nektar++ IO performance for cray XC architecture*, in: *Cray User Group Proceedings*, Stockholm, Sweden, 2018.
- C. Chevalier, F. Pellegrini, *Parallel Comput.* 34 (6–8) (2008) 318–331.
- W.J. Schroeder, B. Lorenzen, K. Martin, *The Visualization Toolkit: an Object-Oriented Approach to 3D Graphics*, Kitware, 2004.
- J. Ahrens, B. Geveci, C. Law, *Vis. Handb.* 717 (2005).
- K. Lackhove, *Hybrid Noise Simulation for Enclosed Configurations* (Doctoral thesis), Technische Universität Darmstadt, 2018.
- M. Germano, *Phys. Fluids* 29 (6) (1986) 1755, <http://dx.doi.org/10.1063/1.865649>.
- A. Refloch, B. Courbet, A. Murrone, C. Laurent, J. Troyes, G. Chaineray, J.B. Dargaud, F. Vuillot, *AerospaceLab* (2011).
- F. Duchaine, S. Jauré, D. Poitou, E. Quémerais, G. Staffelbach, T. Morel, L. Gicquel, *Comput. Sci. Discov.* 8 (1) (2015) <http://dx.doi.org/10.1088/1749-4699/8/1/015003>.
- D. Abrahams, R.W. Grosse-Kunstleve, O. Overloading, *CC Plus Plus Users J.* 21 (7) (2003) 29–36.
- P. Peterson, *Int. J. Comput. Sci. Eng.* 4 (4) (2009) 296–305.
- D.M. Beazley, et al., *Tcl/Tk Workshop*, 1996, p. 43.
- Élie Cartan, *Riemannian Geometry in an Orthogonal Frame*, World Scientific Pub. Co. Inc., 2002.
- Élie Cartan, *Geometry of Riemannian Spaces*, Math. Sci. Press, 2001.
- Élie Cartan, *La Théorie Des Groupes Finis Et Continus Et La Géométrie Différentielle Traitées Par La Méthode Du Repère Mobile*, Gauthier-Villars, 1937.
- M. Fels, P.J. Olver, *Acta Appl. Math.* 51 (2) (1998) 161–213.
- P.J. Olver, *Moving Frames – in Geometry, Algebra, Computer Vision, and Numerical Analysis. Foundations of Computational Mathematics*, in: *London Math. Soc. Lecture Note Ser.*, Cambridge Univ. Press, 2001, pp. 267–297.



- [61] O. Faugeras, in: J.L. Mundy, A. Zisserman, D. Forsyth (Eds.), *Cartan's Moving Frame Method and Its Application to the Geometry and Evolution of Curves in the Euclidean, Affine and Projective Planes*, in: *Lecture Notes in Computer Science*, vol. 825, Springer, 1994.
- [62] E. Piuze, J. Sporing, K. Siddiqi, in: S. Ourselin, D. Alexander, D. Westin (Eds.), *Moving Frames for Hair Fiber Reconstruction*, in: *Lecture Notes in Computer Science Book Series*, vol. 9123, Springer, 2015.
- [63] S. Chun, *J. Sci. Comput.* 53 (2) (2012) 268–294.
- [64] S. Chun, *J. Sci. Comput.* 59 (3) (2013) 626–666.
- [65] S. Chun, C. Eskilsson, *J. Comput. Phys.* 333 (2017) 1–23.
- [66] S. Chun, *J. Comput. Phys.* 340 (2017) 85–104.
- [67] S. Chun, J. Marcon, J. Peiró, S.J. Sherwin, submitted for publication.
- [68] S. Chun, C. Cantwell, in preparation.
- [69] D. Moxey, C.D. Cantwell, G. Mengaldo, D. Serson, D. Ekelschot, J. Peiró, S.J. Sherwin, R.M. Kirby, in: M.L. Bittencourt, N.A. Dumont, J.S. Hesthaven (Eds.), *Spectral and High Order Methods for Partial Differential Equations ICOSAHOM 2016*, Springer International Publishing, 2017, pp. 63–79.
- [70] P.-O. Persson, J. Peraire, 44th AIAA Aerospace Sciences Meeting and Exhibit, 2006, p. 112.
- [71] D. Serson, J.R. Meneghini, S.J. Sherwin, *J. Comput. Phys.* 316 (2016) 243–254.
- [72] D. Serson, J.R. Meneghini, S.J. Sherwin, *Comput. & Fluids* 146 (2017) 117–124.
- [73] D. Serson, J.R. Meneghini, S.J. Sherwin, *J. Fluid Mech.* 826 (2017) 714–731.
- [74] S.J. Sherwin, J. Peiró, *Internat. J. Numer. Methods Engrg.* 53 (2002) 207–223.
- [75] D. Moxey, M.D. Green, S.J. Sherwin, J. Peiró, *Comput. Methods Appl. Mech. Engrg.* 283 (2015) 636–650, <http://dx.doi.org/10.1016/j.cma.2014.09.019>.
- [76] D. Moxey, M.D. Green, S.J. Sherwin, J. Peiró, *New Challenges in Grid Generation and Adaptivity for Scientific Computing*, Springer, 2015, pp. 203–215.
- [77] M. Turner, D. Moxey, J. Peiró, M. Gammon, C. Pollard, H. Bucklow, *Procedia Eng.* 203 (2017) 206–218, <http://dx.doi.org/10.1016/j.proeng.2017.09.808>.
- [78] *Open Cascade SAS*, Open Cascade, 2019.
- [79] J. Marcon, M. Turner, J. Peiró, D. Moxey, C. Pollard, H. Bucklow, M. Gammon, 2018 AIAA Aerospace Sciences Meeting, American Institute of Aeronautics and Astronautics, Reston, Virginia, 2018, p. 1403, <http://dx.doi.org/10.2514/6.2018-1403>.
- [80] C. Geuzaine, J.-F. Remacle, *Internat. J. Numer. Methods Engrg.* 79 (11) (2009) 1309–1331, <http://dx.doi.org/10.1002/nme.2579>.
- [81] T. Colonius, S.K. Lele, *Prog. Aerosp. Sci.* 40 (6) (2004) 345–416, <http://dx.doi.org/10.1016/j.paerosci.2004.09.001>.
- [82] C.K.W. Tam, *Fluid Dyn. Res.* 38 (9) (2006) 591–615, <http://dx.doi.org/10.1016/j.fluiddyn.2006.03.006>.
- [83] R. Ewert, W. Schröder, *J. Comput. Phys.* 188 (2) (2003) 365–398, [http://dx.doi.org/10.1016/S0021-9991\(03\)00168-2](http://dx.doi.org/10.1016/S0021-9991(03)00168-2).
- [84] E.-A. Müller, F. Obermeier, *AGARD CP-22*, 1967, pp. 21–22.
- [85] J. Chaplin, P. Bearman, Y. Cheng, E. Fontaine, J. Graham, K. Herfjord, F.H. Huarte, M. Isherwood, K. Lambrakos, C. Larsen, et al., *J. Fluids Struct.* 21 (1) (2005) 25–40.
- [86] R. Willden, J. Graham, *J. Fluids Struct.* 15 (3) (2001) 659–669.
- [87] Y. Bao, R. Palacios, M. Graham, S. Sherwin, *J. Comput. Phys.* 321 (2016) 1079–1097.
- [88] D. Newman, G. Karniadakis, *J. Fluid Mech.* 344 (1997) 95–136.
- [89] G.M. Laskowski, J. Kopriva, V. Michelassi, S. Shankaran, U. Paliath, R. Bhaskaran, Q. Wang, C. Talnikar, Z.J. Wang, F. Jia, Future directions of high fidelity CFD for aerothermal turbomachinery analysis and design, in: 46th AIAA Fluid Dynamics Conference, Washington, D.C., USA, 2016, pp. 1–30.
- [90] E. Tadmor, *SIAM J. Numer. Anal.* 26 (1) (1989) 30–44.
- [91] A. Cassinelli, F. Montomoli, P. Adami, S.J. Sherwin, *High Fidelity Spectral/hp Element Methods for Turbomachinery*, ASME Paper No. GT2018-75733, 2018, pp. 1–12.
- [92] G.E. Karniadakis, M. Israeli, S.A. Orszag, *J. Comput. Phys.* 97 (2) (1991) 414–443.
- [93] S. Dong, G.E. Karniadakis, C. Chrysosostomidis, *J. Comput. Phys.* 261 (2014) 83–105.
- [94] A. Cassinelli, H. Xu, F. Montomoli, P. Adami, R. Vazquez Diaz, S.J. Sherwin, On the Effect of Inflow Disturbances on the Flow Past a Linear LPT vane using spectral/hp element methods, ASME Paper No. GT2019-91622, 2019, pp. 1–12.
- [95] G. Degrez, C. Boccadoro, J. Wendt, *J. Fluid Mech.* 177 (1987) 247–263.
- [96] J.-P. Boin, J. Robinet, C. Corre, H. Deniau, *Theor. Comput. Fluid Dyn.* 20 (3) (2006) 163–180.
- [97] F.M. White, *Viscous Fluid Flow*, McGraw-Hill New York, 2006.
- [98] G. Mengaldo, D. De Grazia, F. Witherden, A. Farrington, P. Vincent, S. Sherwin, J. Peiro, 7th AIAA Theoretical Fluid Mechanics Conference, 2014, p. 2923.
- [99] E. Eckert, *J. Aeronaut. Sci.* 22 (8) (1955) 585–587.
- [100] J. Eichstädt, M. Green, M. Turner, J. Peiró, D. Moxey, *Comput. Phys. Comm.* 229 (2018) 36–53.
- [101] J. Eichstädt, M. Vymazal, D. Moxey, J. Peiró, *Comput. Phys. Commun.* (2019) submitted for publication.